Title
Characterization of Fuel-Cell Diffusion Media

Author
Gunterman, Haluna Penelope Frances

Publication Date
2011

Peer reviewed|Thesis/dissertation

Characterization of Fuel-Cell Diffusion Media

by

Haluna Penelope Frances Gunterman

A dissertation submitted in partial satisfaction of the
requirements for the degree of
Doctor of Philosophy
in
Chemical Engineering
and the Designated Emphasis
in
Energy Science and Technology
in the
Graduate Division
of the
University of California, Berkeley

Committee in charge:
Professor John Newman, Chair
Professor Elton Cairns
Professor Garrison Sposito

Fall 2011

Abstract

Characterization of Fuel-Cell Diffusion Media
by
Haluna Penelope Frances Gunterman
Doctor of Philosophy in Chemical Engineering
Designated Emphasis in Energy Science and Technology
University of California, Berkeley
Professor John Newman, Chair

Achieving proper water management in polymer-electrolyte fuel cells (PEFC) is an ongoing challenge. Current quantitative treatments of two-phase flow in fuel-cell diffusion media (DM) often assume saturation-dependent transport relations. However, these relations are not validated for the complex physical and chemical structure of the DM, and therefore lack predictive capabilities. Characterization of DM and their water-uptake profiles enables a fundamental understanding of the driving forces behind flooding and facilitates targeted improvement in the form of physically representative simulations. The objective of this work is to characterize, analyze, and explain the wettability and water-uptake behavior of fuel-cell components, namely the DM and catalyst layer (CL), based on manufacturing parameters and physiochemical structure, e.g., fiber structure and hydrophobic treatment of the DM, and chemical composition and crack formation of the CL.

A combination of capillary-pressure saturation (P_C-S) measurements, visual-imaging, and physical-characterization techniques is used to quantify water-uptake behavior and identify causal factors. On an intuitive level, Pc-S curves show the propensity of a material to uptake or eject water. The P_C-S curves demonstrate that DM are neutrally wetting materials that neither spontaneously imbibe nor eject water. DM from various manufacturers exhibit signature features that can be explained partially by visual differences in fiber structure and deposition of a hydrophobic agent, polytetrafluoroethylene (PTFE). Although the initial addition of PTFE improves hydrophobicity of the sample, increasing PTFE loading does not show significant improvements and instead, as evidenced by pore-size-distribution (PSD) measurements, decreases porosity. Systematic studies of the PSDs demonstrate the level of variation that exists within DM and between DM produced by different manufacturers.

To date, there have not been data on the wettability and water-uptake behavior of CLs. Isolated CLs were made in-house and commercially and tested for their P_C-S response. CLs have the propensity to be highly hydrophilic and require capillary pressures as low as -80 kPa to eject water. The presence of Pt or surface cracks increases hydrophilicity. These findings suggest that saturation in CLs, especially cracked CLs, may exacerbate poor transport.

Lastly, this work includes early-stage development of a limiting-current measurement that can be used to calculate effective transport properties as a function of saturation. Results indicate that the method is valid, and different DM have higher transport depending on the operating condition. The technique is yet in a formative stage, and this work includes advice and recommendations for operation and design improvements.

Table of Contents

List of Figures

List of Tables

List of Acronyms

CL	catalyst layer
CV	cyclic voltammagram/voltammetry
DM	diffusion medium/media
DVS	dynamic vapor sorption
EDX	energy dispersive X-ray
FC	fuel cell
FIB	focused-ion beam
GC	gas chromatography
GDL	gas-diffusion layer
LANL	Los Alamos National Laboratory
MEA	membrane-electrode assembly
MIP	mercury intrusion porosimetry
MPL	microporous layer
MRC	Mitsubishi Rayon Corporation
PE(M)	polymer-electrolyte (membrane)
PSD	pore-size distribution
PTFE	polytetrafluoroethylene
PVDF	polyvinylidene fluoride
RH	relative humidity
SGL	Sigracet gas-diffusion layer
USBM	US Bureau of Mines
WTP	water transport plate

Acknowledgements

Professor Newman, Adam Weber, Jeff Gostick, and Anthony Kwong are due a level of appreciation best expressed in person.

The aid and support of the Newman lab, Weber lab, and Los Alamos National Laboratory Fuel Cell Team is gratefully acknowledged.

This work was supported by the Assistant Secretary for Energy Efficiency and Renewable Energy, Office of Fuel Cell Technologies, of the U.S. Department of Energy under contract number DE-AC02-05CH11231.

Chapter 1.

1.1 Introduction

The polymer-electrolyte fuel cell (PEFC) is a device that converts hydrogen and oxygen to water and electrical energy. Despite the attractiveness of an energy device that produces water, poor water management in PEFCs limits the performance, durability, and market feasibility of fuel cells. Proper water management in PEFCs involves a trade-off between overdrying the membrane component of the cell, which causes both gas cross-over and poor conduction, and flooding the two-phase region of the cell, which leads to reactant starvation. There is interest in understanding how physical properties of the cell materials affect the water uptake, and hence flooding tendencies, of PEFCs in order to improve reactant and product transport.

A PEFC is a multi-layer, multi-phase system capable of electrical energy generation. For reference of scale, a PEFC the size of a shoebox is capable of generating roughly 2 kW.[1] Operating conditions are 60 to 80°C with humidified gases to prevent overdrying of the polymer-electrolyte membrane, a central feature of the PEFC. Further details of PEFC components are shown in Figure 1.1. On the far sides are metal plates that act as both gas channels and current collectors. Moving inward are the diffusion media that are conductive and also enable gas to diffuse evenly to make full use of the catalytic surfaces. The diffusion media contact the catalytic surfaces of the anode and cathode, where electrochemical oxidation and reduction occur, respectively. These electrodes sandwich the polymer-electrolyte membrane, typically Nafion® from Dupont. The membrane is ionically conducting, thereby allowing protons to move across the membrane, but electronically insulating. Electrons flow externally from anode to cathode, thus generating electricity. The reactions are given as follows:

Anode: $2H_2 \rightarrow 4H^+ + 4e^-$
Cathode: $O_2 + 4H^+ + 4e^- \rightarrow 2H_2O$
Net reaction: $2H_2 + O_2 \rightarrow 2H_2O$

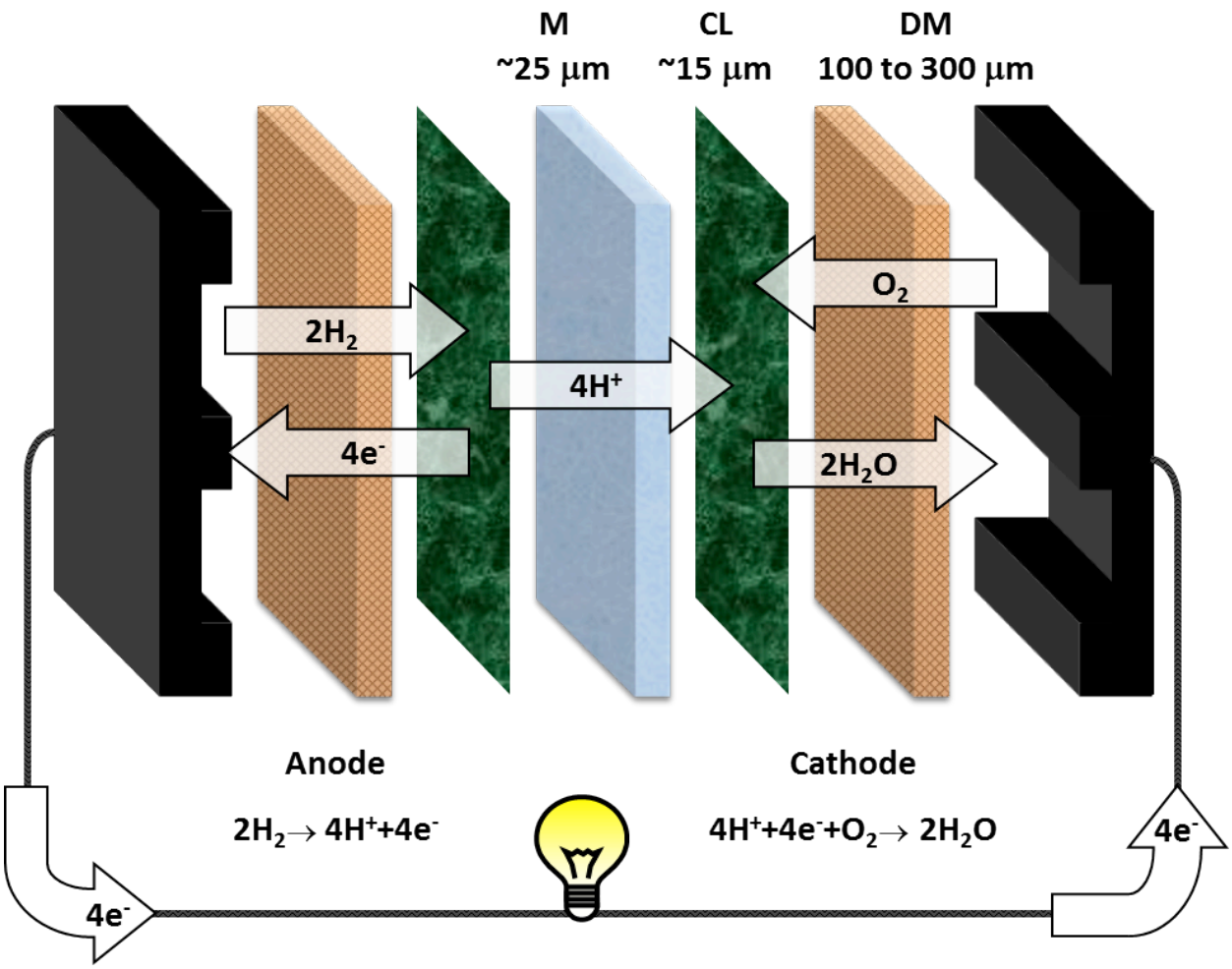

Figure 1.1. Expanded view of a PEFC that shows the metal plates (black) that serve as gas channels and current collectors, the diffusion media (DM), catalyst layers (CL), and polymer-electrolyte membrane (M).

The upper bound of elevated-temperature operation stems from the membrane's need to remain hydrated to retain ionic conduction and prevent gas cross-over. Conditions required for proper membrane function therefore overlap with conditions for liquid water accumulation. Water can build up in the system, particularly on the cathode side on which it is produced, leading to reactant starvation and cell shutdown. Significant work has focused on altering and modeling the diffusion media in particular as a means of understanding and controlling water uptake and retention properties.[2-5] The following work develops this more fully.

The diffusion media in PEFCs are comprised of a gas-diffusion layer (GDL) that is often accompanied by a microporous layer (MPL). The GDL is made of carbon fibers that are either woven or pressed to form a porous network. The layer is then treated with a polytetrafluoroethylene, PTFE, $-(CF_2)_n-$, solution to create a nanometer-scale hydrophobic layer of PTFE on the otherwise hydrophilic carbon fibers. The purpose of the GDL is to provide a porous structure that conducts electrons through the solid and allows reactants and products to

move through the void space. Typical GDLs are made of 10 μm diameter fibers stacked to be 100 to 300 μm thick with 70 to 80% porosity. Standard PTFE loadings in the GDL are 5 to 20 wt%. MPLs have also been added to GDLs to create a thinner, <50 μm, region between the GDL and catalyst layer that consists of smaller, more hydrophobic pores. The MPL is added with the intent of discouraging liquid water build-up near the catalyst layer, decreasing contact resistance between the GDL and CL, and providing a structural barrier to protect the membrane from the GDL carbon fibers that can pierce the membrane and lead to gas cross-over.[6-8] Standard PTFE loadings in the MPL are higher than that in GDLs and range from 20 to 30 wt% PTFE. MPLs have improved PEFC performance consistently in experiments, with initial empirical optimizations demonstrating increased peak power for composite diffusion media that balance the strengths of high gas permeability and hydrophobicity.[9-13] MPL traits that lead to better performance include higher hydrophobicity,[9, 10, 14] thinner layers,[15] and micrometer-sized pores.[16] For clarification purposes, note that colloquial usage of "GDL" may refer to a GDL with or without a MPL.

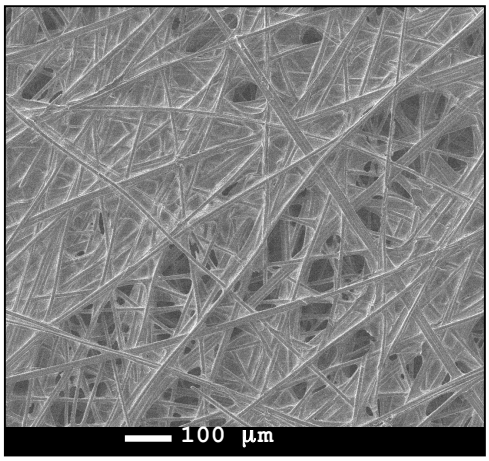

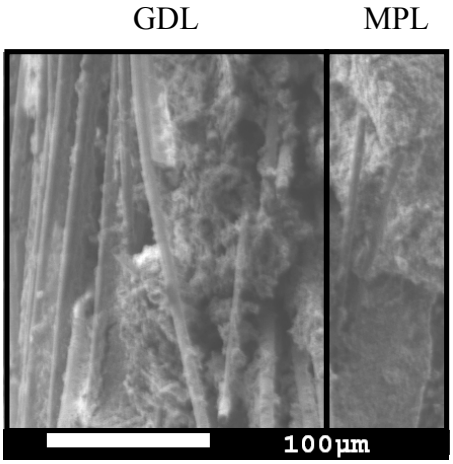

a. Toray 120 20% PTFE b. Sigracet 5% GDL, 23% MPL

Figure 1.2. a. Image of a GDL that shows a porous fibrous structure formed with carbon fibers, binder, and PTFE.
b. Cross-section of a diffusion medium with a GDL and MPL. The MPL material is denser than the GDL material and has a clay-like appearance.

Gas that diffuses across the GDL and MPL reaches the catalyst layer (CL). The CL is the thinnest layer at 10 to 20 μm and is comprised of catalyst particles, typically Pt supported on carbon, held together with polymer-electrolyte binder. The CL is fused to the membrane to ensure ionic conductivity of protons to the cathode where they combine with oxygen to produce water and electrons. The presence of the polymer-electrolyte in the CL complicates the attempt to study independently the CL, but some initial forays into CL characterization are discussed in a subsequent chapter.

1.2 Theory and Application

The overarching objective in fuel-cell studies is to create a better fuel cell. To achieve this, the operating conditions and materials require optimization. Optimization is facilitated through the use of simulations that enable rapid prototype testing and promote directed development of improved materials. In turn, the simulations require accurate material wetting properties and transport parameters. The remainder of the introduction provides a broader context of this work and addresses the following: why two-phase effects impact transport phenomena, how these effects are incorporated into present models, and where this work fits toward tailoring physiochemical factors to optimize water management and transport behavior.

1.2.1 Governing Equations

The main governing equations in macrohomogeneous models are Darcy's law,[17] which solves for fluid movement in porous media, Stefan-Maxwell convection and diffusion,[18] which govern gas flow, Ohm's law,[19] which governs current, and the energy equation,[18] which governs temperature profiles. The transport coefficients in Darcy's law and the Stefan-Maxwell expressions require saturation corrections to capture the resultant change in resistance to liquid and gas flow depending on the saturation.

Liquid water generated at the cathode is assumed to be transported out according to Darcy's law. Darcy's law for porous media relates the gradient in pressure, viscosity of the fluid, and permeability of the medium to the resulting fluid velocity, u_L, as shown below,

$$u_L = \frac{-k}{\mu} \nabla P_L ,$$

where k is the permeability of the diffusion layer, μ is the water viscosity, and P_L is the liquid pressure. Measuring k in a single-phase system for a GDL is reasonably straightforward, although theoretically and experimentally obtained values may vary.[20-29] A flow rate is set across the GDL, and the resulting pressure gradient is measured to enable calculation of k. However, the permeability of a system during fuel-cell operation depends not only on geometry and microstructure, but also saturation. In the case of water in the GDL, the more saturated the GDL, the more connected the water pathways, and the more permeable the GDL to water. The effective permeability, k_{eff}, is often divided into single- and two-phase contributions as follows,

$$k_{eff} = k_{abs} \cdot k_{rel}$$

where k_{abs} is the single-phase permeability and k_{rel} is a relative permeability that depends on saturation. k_{rel} can be estimated from a simple constitutive relation or complex model.[17, 30, 31] A discussion follows regarding the strengths and weaknesses of using a simple or complex relationship. Regardless of the analytical approach, calculation of the effective permeability for simulation purposes necessitates saturation information.

The Stefan-Maxwell relation, which is used to determine gas-phase multicomponent transport, also contains saturation dependence in the effective diffusion coefficient. For a system with N species, the Stefan-Maxwell relation states that

$$\nabla x_i = \sum_{\substack{j=1 \\ j \neq i}}^{N} \frac{x_i x_j (\boldsymbol{v}_j - \boldsymbol{v}_i)}{D_{ij}}$$

where x_i is the mole fraction of species i, $\boldsymbol{v}_i$ is the velocity, and D_{ij} is the binary diffusion coefficient. Traditionally, the diffusion coefficient is subdivided into separate pieces for a porous system as follows:

$$D_{eff} = \frac{\varepsilon}{\tau} D,$$

where ε is the porosity, τ is the tortuosity, and D_{eff} is the single-phase diffusion coefficient. Passage through the material is easier at higher porosity or lower tortuosity, and ε/τ ranges from 0 for a solid material to 1 for open space. Although inconsistent with the definition of k_{eff}, which includes saturation, the traditional nomenclature of D_{eff} as a single-phase diffusivity is retained for historical reasons. When simulating transport in DM, the diffusion coefficient will be affected by saturation because water changes the gas-phase pore space. Constitutive relations are used to correct for saturation effects.

1.2.2 Implementation

Fuel-cell simulations incorporate saturation-dependent transport properties at different levels of complexity. There is a trade-off between simplicity and detail in approximating the fibrous structure and complex fluid-advancement pattern. However, increasing the complexity of a model does not necessarily make it more useful. Regardless of the approach, there is use and need for fundamental experimental data to validate and improve these simulations, and to contribute toward a physical intuition of what is occurring in the system.[32] The end product should provide a predictive relationship for transport properties as a function of saturation, manufacturing properties, and operating conditions. Several extensive reviews have discussed modeling water transport in PEFCs and DM.[2-5] The review by Weber et al. includes treatment of the effects of compression, anisotropy, and full-cell assembly on DM structure and water transport.[2] For purposes of providing a basic motivation of this work, some methods for including saturation effects are discussed briefly in terms of their strengths and weaknesses.

The most general treatment of saturation effects is through constitutive equations. Common expressions include S^n or $(1-S)^n$ terms, where S is saturation and n is a theoretically or empirically determined exponent. The Wyllie expression, in which n=3, is based on a cut-and-rejoin model of tubes and is widely used due to its simple form.[17] Some microscopic simulations and experimental fits have suggested n-values that range from 2 to 5.[33-40] Many more constitutive relations have been proposed, including the Bruggeman,[41] Corey,[42] Brooks-Corey,[43] and Van Genuchten[44] expressions. These simple relations are easy to implement and attempt to capture the average fluid transport through the use of a bulk-flow parameter. However, because they were developed in the context of soil science and oil reclamation, the expressions are not customized for fibrous systems in general, nor for the GDL in particular. Because these basic constitutive relations do not include medium-specific parameters, they lack predictive capabilities for determining transport properties as a function of manufacturing specifications, such as thickness or PTFE loading.

A slightly more customized, but still easily executed, means of incorporating saturation-dependence is to use idealized pore and contact-angle approximations to calculate the relative transport parameter. Of particular interest for porous-medium studies is the relationship between pore-filling and capillary pressure (P_C), defined in fuel-cell systems as the liquid pressure minus the gas pressure. Higher P_C increases the driving force to fill a pore with liquid whereas lower P_C increases the driving force to fill a pore with gas. P_C can be related to the contact angle according to the Washburn version of the Young-Laplace equation as seen below:[17]

$$P_C = P_L - P_G = \frac{2\gamma \cos\theta}{r},$$

where P_L is liquid pressure, P_G is gas pressure, γ is surface tension, θ is contact angle, and r is the pore radius. Intuitively, based on how P_C has been defined as $P_L - P_G$, the higher the capillary pressure, the more dominant the liquid phase, and the higher the water saturation. Because the cosine term is negative for hydrophilic materials and positive for hydrophobic materials, and because P_C is inversely related to pore radius, a general rule of thumb is as follows: as P_C increases, the small hydrophilic pores fill first, followed in order by large hydrophilic pores, large hydrophobic pores, and finally small hydrophobic pores. This expression assumes cylindrical pores and a well-defined contact angle. However, the definition of a pore is unclear in a highly porous, irregularly shaped, interconnected fibrous structure. Some attempts have been made to determine a contact angle for the GDL,[45] but a universal contact angle is challenging to define for a material of mixed wettability with complex surfaces. Instead, the pore radius and contact angle used in the Young-Laplace expression should be considered as an equivalent radius and equivalent contact angle. As a macrohomogeneous expression, the Young-Laplace equation is advantageous for several reasons. First, the language of the field and some of its most fundamental characterization tests, such as mercury-intrusion porosimetry, are cast in terms of these apparent quantities. Second, the concept of an equivalent pore radius and contact angle is intuitive and computationally straightforward; we speak of small and large pores, or hydrophilic and hydrophobic materials. Third, the output from physical measurements can be translated into continuous mathematical expressions with fitting parameters that incorporate GDL properties.[33, 46, 47] However, the fitting parameters are not yet developed sufficiently to offer predictive capabilities. More experimental data and iterative fits are necessary before this type of constitutive equation can forecast effective transport properties based on manufacturing specifications and operating conditions.

The most elaborate method for calculating effective transport is with microscopic models. Microscopic models vary in complexity depending on how they model the structure and liquid-invasion criteria. Pore-network,[48, 49] full-morphology,[50] and Lattice-Boltzmann simulations[51-55] have been extended to multi-phase flow, and their agreement has been discussed in the literature.[56] Pore-network simulations use an idealized network structure in which the transport pathways are interconnected and of varying size.[35, 57] Full-morphology methods use a fibrous microstructure explicitly, but imbibition is idealized to proceed by advancement of spheres.[58] The Lattice-Boltzmann model is the most rigorous and best accounts for interfacial phenomena, but the detail comes at the price of being computationally expensive and is dependent on grid spacing.[48, 53, 54, 56] The advantage of these models is that they can incorporate better the heterogeneous structure, wettability, and hysteresis of the GDL. However, in addition to being computationally intense, they require more physiochemical information than can be determined

or controlled reasonably by a GDL manufacturer. The microscopic models are more complex, but they are not necessarily more predictive than an adjustable macroscopic model.

An underlying issue in all of these methods for incorporating saturation effects is the need for experimental data to test, validate, and refine the models. Accurate saturation data are necessary, but difficult to obtain directly in-situ. The question becomes how to obtain saturation as a function of other parameters in the system. Of particular interest for porous-medium studies is the relationship between capillary pressure (P_C) and saturation. The most commonly used P_C-saturation (P_C-S) relationship, the Leverett function,[59] is an expression taken from soil-science studies. The Leverett function relates P_C to saturation as show below,

$$P_C = \sigma \cos\theta \sqrt{\frac{\varepsilon}{k}} J(S),$$

where σ is the surface tension, θ is the contact angle, ε is the porosity, S is saturation, and J(S) is found empirically. The most common J(S) function was defined by Udell[60] to be

$$J(S) = 1.417(1-S) - 2.120(1-S)^2 + 1.263(1-S)^3 \text{ for } \theta < 90° \text{ and}$$
$$J(S) = 1.417S - 2.120S^2 + 1.263S^3 \text{ , for } \theta > 90°.$$

The applicability of the Leverett function to GDLs is debatable.[23, 61] The Leverett approach was developed for an isotropic soil of uniform wettability and low porosity, <30%. Meanwhile, a standard diffusion medium is anisotropic, of mixed wettability due to nonuniform PTFE coating, and has a high porosity, >70%. Another limitation of the Leverett approach is that the square-root term does not scale across systems of varying topology.[17] Due to these considerations, there is interest in obtaining experimentally diffusion-medium-specific P_C-S relationships.

This work discusses how to measure and analyze P_C-S curves for fuel-cell DM. In its simplest form, this P_C-S data can be incorporated directly into constitutive relations and improve simulations by providing accurate saturation data. A customized simulation can use this P_C-S analysis to determine fitting parameters and identify which manufacturing properties alter the transport parameters. Complex microscale simulations can use this data to validate the performance of their model and determine the level of detail necessary to match physical data. The objective is to understand how manufacturing characteristics, e.g., thickness and PTFE loading, impact physical measurables, e.g., P_C-S and porosimetry results, that affect two-phase behavior in fuel cells. Characterizing the relationship contributes toward an understanding of what factors dictate flow in heterogeneous media, and how to tailor materials to suit complex needs.

The remainder of this work is divided into three sections: first, a detailed discussion of P_C-S results as measured for the GDL and CL; second, visual and physical characterizations of the materials and consideration of their role in explaining the previous results; lastly, development of an alternative saturation relationship that attempts to bypass P_C-S calculations by determining transport properties as a direct function of saturation.

Chapter 2.

2.1 Capillary Pressure versus Saturation Measurements

Capillary-pressure (P_C) effects play a major role in fuel-cell components such as the gas-diffusion layer (GDL), microporous layer (MPL), and catalyst layer (CL) owing to the abundance of pores with diameters in the micrometer range that make capillarity significant. One water-uptake characterization is the P_C-saturation (P_C-S) curve, in which P_C is defined as[17]

$$P_C = P_{NW} - P_W$$

where P_{NW} is the pressure of the nonwetting fluid and P_W is the pressure of the wetting fluid. From a P_C -S curve, the saturation of the medium at a given P_C can be determined and used to understand the propensity for a material to take up or eject fluid. Most fuel-cell materials are hydrophobic, i.e., water is the nonwetting fluid and air is the wetting fluid. Therefore, P_C for fuel-cell systems is defined as

$$P_C = P_L - P_G$$

where P_L is liquid pressure and P_G is gas pressure. Intuitively, based on how P_C has been defined, the higher the capillary pressure, the more dominant the liquid phase, and the higher the water saturation.

The shape of the P_C-S curve provides insight into the wettability and pore characteristics of a material. A simplified diagram is shown in Figure 2.1a. First, the horizontal location of the curve demonstrates whether the material is wetting (lies in the negative P_C range), nonwetting (positive P_C range), or neutral (straddles the zero-P_C line). Second, the shape of the curve gives information on the pore characteristics; if there is a large change in saturation at a specific P_C, then the pores are predominantly of one type whereas if there is a more gradual change, then the pores are of more broadly distributed size or contact angle. Third, the vertical location of the curve, most notably on the lower range of the curve, indicates whether there is an irreducible

saturation past which liquid cannot be pulled out. This will occur when water becomes stranded in the material and there is not a connected fluid phase by which to remove the remaining water.

There are two types of hysteresis that may be visible on a P_C-S curve. If the P_C-S curve is divided into an injection and a withdrawal segment, the injection segment is seen to be to the right of the withdrawal segment as shown in Figure 2.1a. This is because of a difference between an advancing and receding contact angle as shown in Figure 2.1b.[62, 63] The advancing contact angle is larger than the receding contact angle, and thus the fluid appears to be more nonwetting. A higher P_C is necessary to reach a certain saturation, and the material behaves more hydrophobicly during injection than withdrawal. The other type of hysteresis is between the primary and subsequent P_C cycles because the first time a sample is wetted, the sample will start from zero saturation. Subsequent cycles will start from a higher saturation if there exists an irreducible-saturation limitation. Subsequent injection cycles may lie at saturations above the primary injection curve.

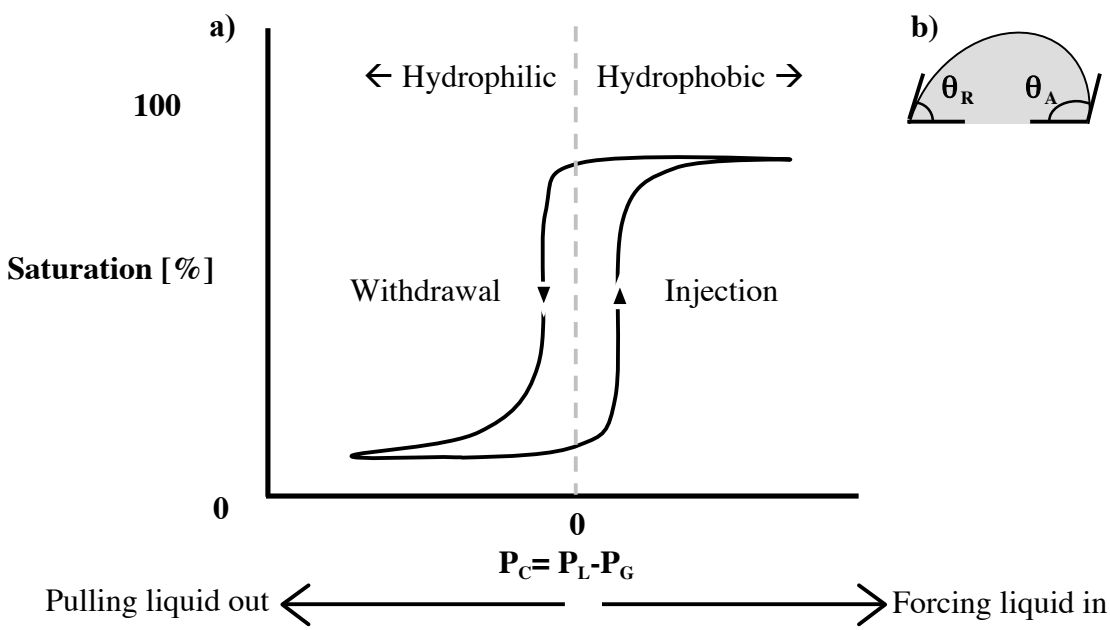

Figure 2.1. a) Illustration of a secondary P_C-S curve for a neutrally wetting material. Curves for hydrophobic materials would be shifted toward the right while curves for hydrophilic materials would be shifted toward the left. b) Hysteresis between the injection and withdrawal curves is due to the difference in contact angle depending on whether the fluid is advancing (larger contact angle) or receding (smaller contact angle) during injection and withdrawal, respectively.

Having discussed the information gained from P_C-S curves and their interpretation, we next consider how these curves are determined. As far as determination of P_C-S relationships for fuel-cell materials is concerned, most studies have focused on gas-diffusion layers (GDLs). Thus we start with the discussion of how to obtain a P_C-S curve measurement for GDLs and later treat design considerations for testing the catalyst layer (CL).

P_C can be controlled by altering either P_G or P_L. A diagram of the set-up for each method (gas- or liquid-controlled) is shown in Figure 2.2. The steps for implementation and post processing are outlined in Figures 2.3 and 2.4. The design of the gas-controlled method is modeled after the work of Gostick et al.[61] In the case of a gas-controlled method, P_G is varied while P_L is kept constant. The liquid side of the set-up is connected to a water reservoir, and the mass of the water in the reservoir is recorded to determine the amount of water that has entered the sample. The connections are carefully primed so that air bubbles that may impede fluid transfer between the sample and the reservoir are not trapped in the tubing. Suction is maintained on the liquid side of the rig via a liquid tube that hangs below the sample height. The sample is sandwiched between hydrophilic and hydrophobic membranes to create an isolated 2-phase region. A key point during preparation is to maintain liquid suction until the run is ready to begin so that the sample remains in a dry condition before the run and also to establish a zero-saturation baseline. The easiest blunder is to close off suction from the liquid side and expose the sample to the liquid pressure at the water reservoir on the balance; the liquid pressure at the balance typically is close to zero hydraulic pressure, thereby exposing the sample to zero instead of negative P_C. If P_C is near zero, uptake may occur. The trick is to increase P_G, thus decreasing P_C, in preparation for switching the liquid side from pulling suction to going to the reservoir and increasing P_C. Pressure values are specified in an input file, and a syringe pump advances or retracts to move from one pressure value to another. When choosing pressure values for the gas-controlled method, the objective is to include enough points in regions of interest to capture key features of the curve, such as where uptake occurs or any peculiar knees in the data, and also not to linger too long in high P_C (low P_G) regions that may cause significant evaporative loss. Once the desired pressure is achieved, the pump is paused until the mass of the water reservoir stabilizes to ensure steady-state saturation. When both the pressure and mass are stable, both values are recorded, and the run moves on to the next pressure point.

A major advantage of this technique is that data are taken at steady-state. The method is robust to disturbances in the laboratory environment, e.g., doors opening and closing or vibrations to the lab bench due to use of drawers or accidental bumps. For a typical GDL measurement with three cycles between -30 and 30 kPa, the run time is roughly 8 hours. Over the course of the run, there will be a small amount of water loss from the reservoir due to evaporation. Evaporative effects are easily accounted for by entering evaporation-rate estimates until the three curves lie on top of each other; if the evaporation rate is too low, the saturation will be read as artificially high, and the curves will appear to creep upward. Evaporation rates are seen to be constant through the course of testing. If an extended run is desired and if the evaporation rate is seen to change between night and day, a second evaporation rate can be implemented in a similar fashion. Measurement in the negative Pc range is best achieved with the gas-controlled method. The gas-controlled method is limited in the positive P_C range by the level of vacuum that can be held by the system tubing and the need to consider evaporation rates; data points in the high-P_C range are kept to minimum levels because evaporation may begin to

differ significantly at the high P_C, low P_G, end from the evaporation rate at the lower end of the tested spectrum. The gas-injection method is thus ideal for measurement of hydrophilic or neutrally wetting materials.

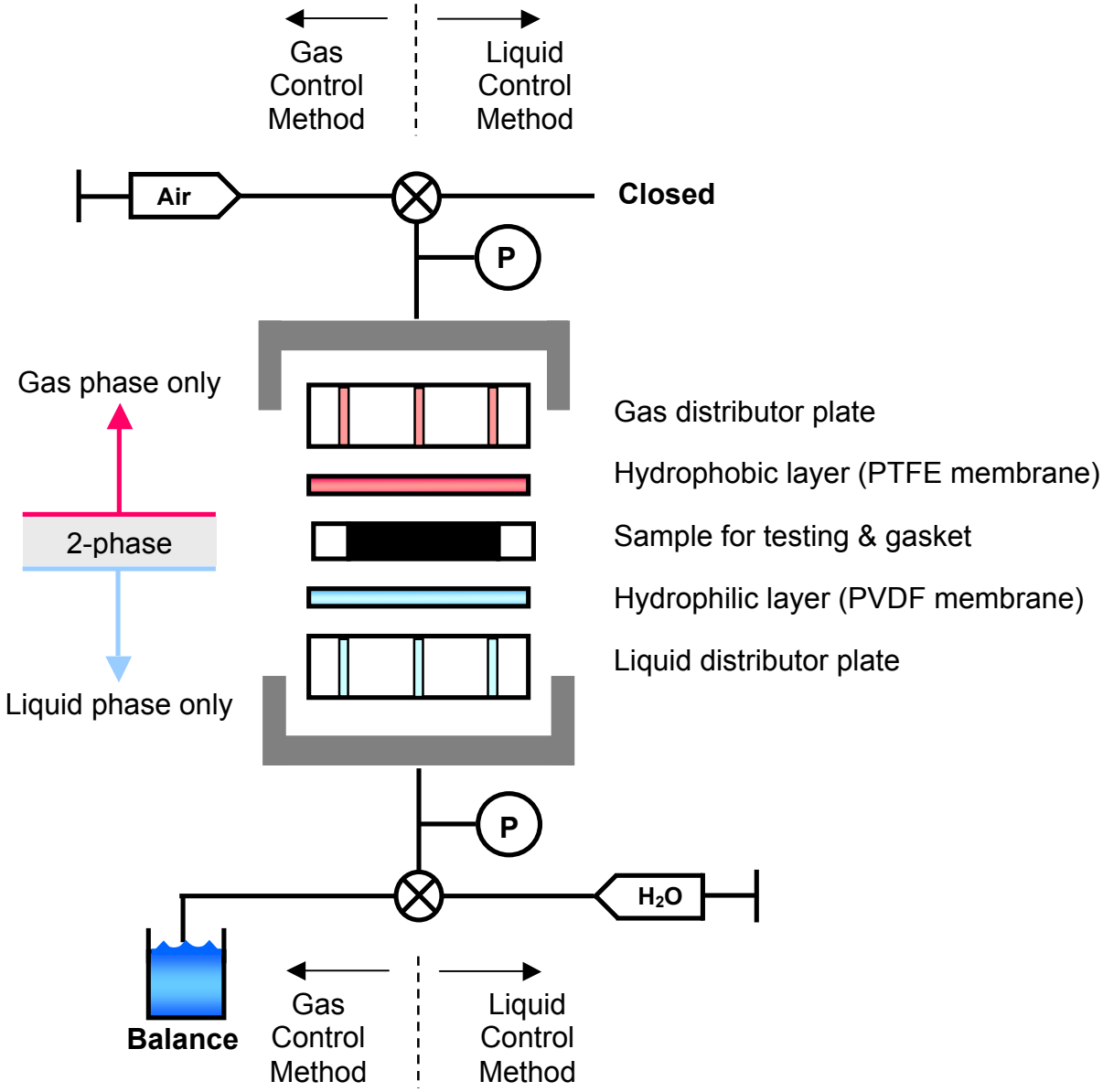

Gas Control	
Pros	• Provides P_C-S steady-state • No limit on negative P_C
Cons	• Time consuming • Limited to < 1 atm positive P_C

Liquid Control	
Pros	• Slightly faster • No limit on positive P_C
Cons	• Not steady-state • Limited to < 1 atm negative P_C

Figure 2.2. Schematic of P_C-S measurement apparatus showing components for gas- and liquid-controlled P_C. The sample is sandwiched in a 2-phase region with all other areas being a single-phase region. A table of pros and cons for both gas and liquid control is included.

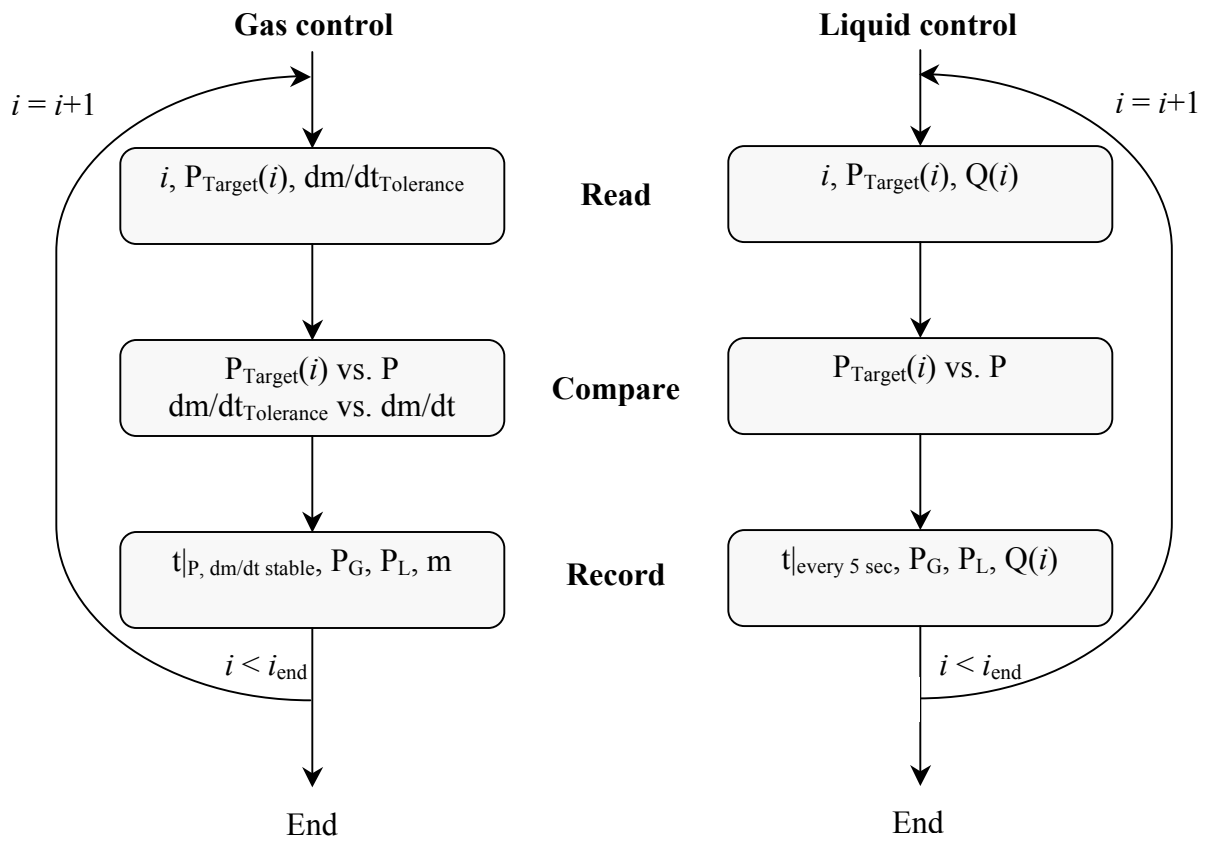

Figure 2.3. Outline of steps implemented in Labview. Variables that are read into the program are listed in the "Read" section with i referring to a counting index, $P_{Target}(i)$ referring to the pressure target at counter i, $Q(i)$ referring to the flow rate used during section i, and $dm/dt_{Tolerance}$ being a global specification of mass stabilization required before taking a data point. The conditions under "Compare" must be met before moving on to "Record." Data in the gas-controlled scenario are logged once both pressure and mass stabilization targets are reached. Data from the liquid-controlled system are recorded every 5 seconds.

Output and post-processing: Gas-controlled system:

Output				Post-processed	
t	**P_L**	**P_G**	**m**	**P_C**	**Saturation**
t_1	P_{L1}	P_{G1}	m_1	P_{L1}- P_{G1}	0
t_2	P_{L2}	P_{G2}	m_2	P_{L2}- P_{G2}	$\frac{m_2 - m_1 + \text{evap.rate} \cdot (t_2 - t_1)}{\text{porosity} \cdot \rho_{H_2O}}$
t_3	P_{L3}	P_{G3}	m_3	P_{L3}- P_{G3}	$\frac{m_3 - m_2 + \text{evap.rate} \cdot (t_3 - t_2)}{\text{porosity} \cdot \rho_{H_2O}}$

Evaporation rate determination:

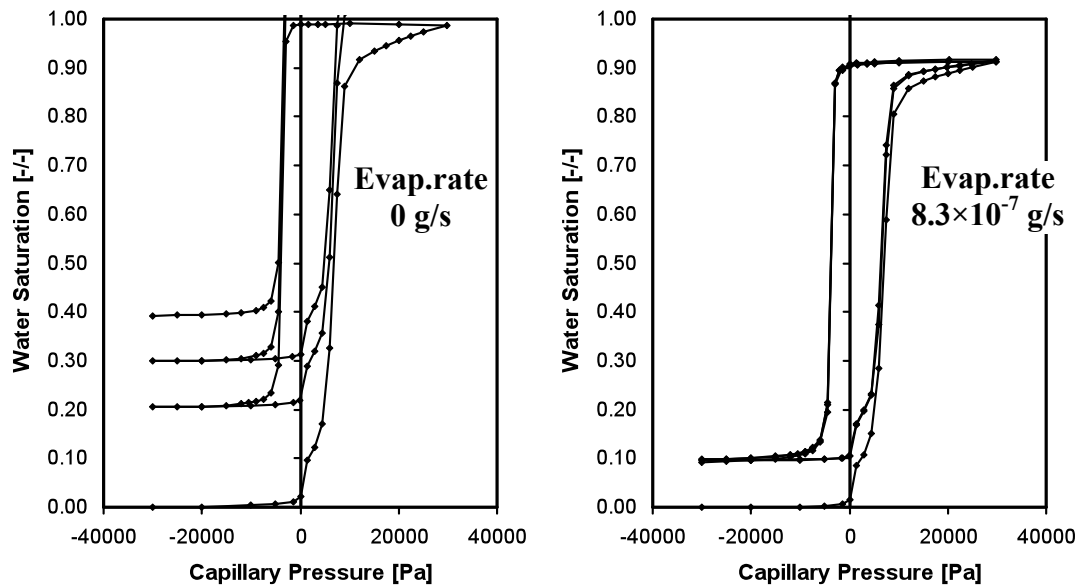

Figure 2.4a. Above: Sample output file and post-processing for gas-controlled system. Using the output data of t (time), P_G, P_L, and m (mass of water reservoir), the P_C-S curve is found for TGPH-120 5%.
Below: An evaporation rate is fit to the experiment such that the curves lie on top of each other. The graph on the left does not take evaporation from the water reservoir into account. Therefore, the saturation is artificially high because the water leaving the reservoir is being recorded as going into the GDL. On the right is a graph of the same data that includes an evaporation rate. The evaporation rate for this particular run is found to be 8.3×10^{-7} g/s.

Output and post-processing: Liquid-controlled system:

Output				Post-processing			
t	**P_L**	**P_G**	**Flow rate**	**V_{Inj}**	**V_{Bub}**	**P_C**	**Saturation**
t_1	P_{L1}	P_{G1}	Q_1	$V_1=0$	V_{Bub_0}	P_{L1}- P_{G1}	0
t_2	P_{L2}	P_{G2}	Q_2	$Q_2(t_2-t_1)+V_1$	$\frac{P_{L_1}}{P_{L_2}} V_{Bub_0}$	P_{L2}- P_{G2}	$\frac{V_2-(V_{Bub_1}-V_{Bub2})-\text{evap.rate}\cdot(t_2-t_1)}{\text{porosity}}$
t_3	P_{L3}	P_{G3}	Q_3	$Q_3(t_3-t_2)+V_2$	$\frac{P_{L_1}}{P_{L_2}} V_{Bub_0}$	P_{L3}- P_{G3}	$\frac{V_3-(V_{Bub_2}-V_{Bub3})-\text{evap.rate}\cdot(t_3-t_2)}{\text{porosity}}$

Initial bubble-size determination:

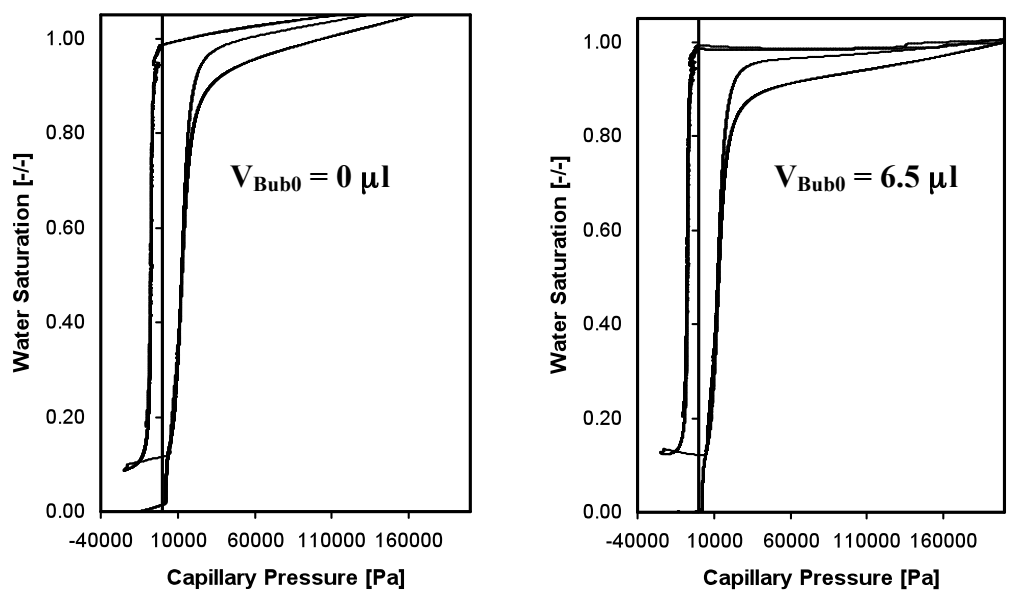

Figure 2.4b. Above: Sample output file and post-processing for liquid-controlled system. Using the output data of t (time), P_G, P_L, and Q (flowrate), the P_C-S curve is found for the Freudenberg H2315 IX53 sample.
Below: A graph before adjusting for the presence of an air bubble is shown on the left. Water saturation is shown to be artificially increasing with P_C, because the injected water is pressing into the volume of an air bubble, not filling additional pores. On the right is a graph that has been adjusted for the presence of an air bubble. The bubble size is increased until the top portion of the curve, the withdrawal section, is flat. The bubble size for this particular run was found to be 6.5 µl.

Implementation of the liquid-injection method is modeled after the work of Harkness et al.[64] In contrast to the gas-injection method in which P_C is controlled, and saturation is measured by the water balance, the liquid-injection method entails controlling the saturation and measuring the resulting P_C. The preparation of the set-up is very similar to the aforementioned approach with particular care taken to ensure that no air bubbles are caught in crevices or connections. The precision of the saturation measurement is dependent on the injected liquid going into the sample and displacing air therein instead of merely compressing or expanding a bubble in the liquid side of the rig. Whereas the suction could be immediately removed for the gas-controlled method, the liquid-injection method requires some time, typically an hour, for the environment within the rig to reach steady state. The difference is because when the suction is closed for the gas-injection run, the water reservoir provides a source for water to evaporate to the gas side of the rig without appreciably affecting liquid pressure. However, when suction is applied to the liquid run, the liquid side becomes a closed system, and any water evaporation or condensation is seen in the form of a steadily decreasing or rising P_L, respectively. Closing the liquid column that provides suction will have no effect on P_L once the system has reached steady state. The input file for the liquid-injection run specifies the upper and lower boundaries of P_C to probe and an injection speed by which to alter the saturation and subsequently alter P_C. A measurement is taken every 5 seconds to record the cumulative injected volume and P_C. Postprocessing of data is similar to that discussed previously of finding an evaporation rate such that the Pc-S curves lie on top of each other. An additional parameter for the liquid-injection method is an initial bubble size. For example, an air bubble in the liquid system manifests itself in the form of a slanted saturation plateau in the upper-P_C range. Data that do not account for an initial air bubble will artificially show an increase in saturation because injected water is compressing a bubble instead of further saturating a fully saturated sample. A simple ideal-gas law relationship can be added to the saturation values. The initial air-bubble volume is adjusted until the 100% and 0% saturation plateaus are flat. This method is capable of accounting for air bubbles less than 10 μl on the liquid side of the rig.

An advantage of the liquid-injection method is that a standard run can be completed in 3 to 5 hours instead of the 8 hours typically necessary for a gas-injection run, thus making the continual measurement method convenient for fast measurements and tracking short-lived injection or ejection events. That said, while lower speeds have typically been cited as leading to reasonable results, we have found the higher-speed runs to behave more erratically and less reproducibly. This may be due to the difference that the gas method is a steady-state measurement, whereas the liquid method is a dynamic measurement. Troubleshooting the liquid-injection run can be challenging because of this additional requirement for all parts and sensors to be robust in the midst of continual movement and power consumption required to accomplish said movement. For reasonably slow injection rates in which full saturation is reached in 1 to 2 hours, agreement between the gas- and liquid-injection runs is good, as can be seen in Figure 2.5. We discuss other variations to the liquid-injection method as published by Harkness in a later section. For now, let it suffice to say that preparing a liquid-injection method requires slightly more finesse because of the sensitivity to air bubbles and reliance on precision of the syringe pump for determination of saturation. The liquid-injection method is best suited for measurements in the positive-Pc range and is limited in the negative range by how much suction can be pulled on the liquid side before the liquid degasses and a gas bubble forms. The

liquid-injection method is thus ideal for measurement of hydrophobic or neutrally wetting materials.

All experiments listed hereafter use a Harvard Apparatus PHD Ultra Infuse/Withdraw syringe pump that is controlled by Labview. The hydrophobic membranes are Sartorius Stedim polytetrafluoroethylene (PTFE) membranes with 0.2 μm pores. The hydrophilic membranes are Durapore Millipore polyvinylidene fluoride (PVDF) membranes with 0.1 μm pores. Omega pressure sensors, model number PX603, were used, although based on a handful of sensor failures, future researchers may wish to procure an Unik 5000, once named Druck, series sensor from GE that were used by Harkness et al.[64]

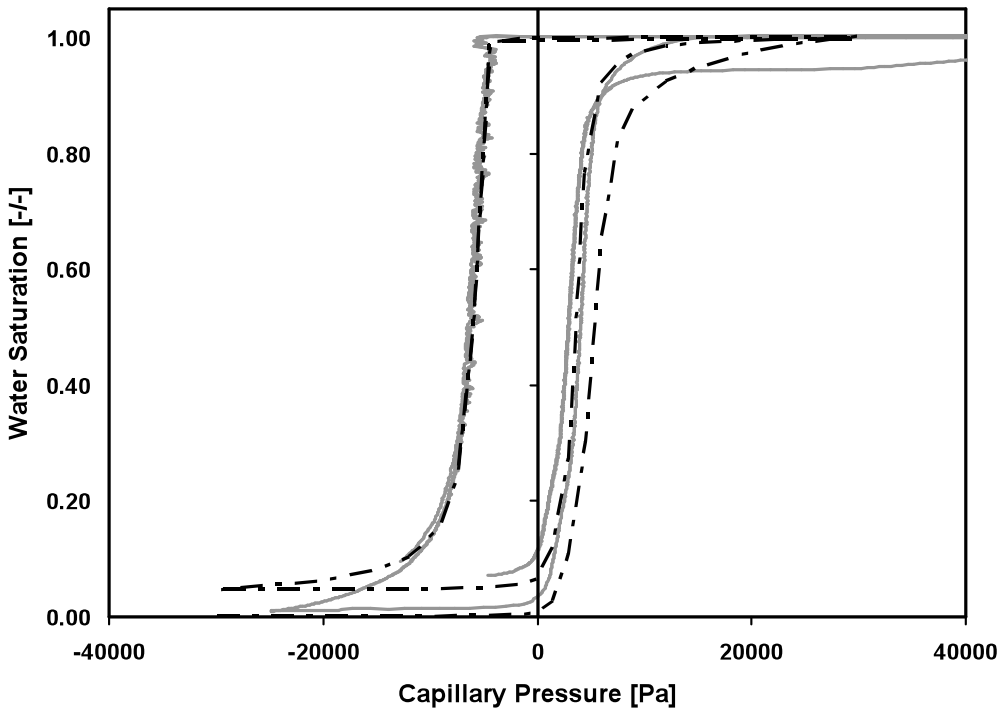

Figure 2.5. P_C-S curves for SGL 24 AA GDL (190 μm thickness, 0% PTFE treatment) determined by the gas-controlled method (black) and liquid-controlled method (grey) run at 1 μl/min. Reasonable agreement is seen between the two methods for secondary curves.

2.2 P_C-S Curves of GDLs

Typical P_C-S curves of GDLs are shown in Figure 2.6. The curves are from GDLs made by SGL, Toray, Freudenberg, and Mitsubishi Rayon Corporation (MRC). The main point is that the curve straddles the zero-Pc line and indicates that the GDLs are neutrally wetting materials.[61, 63, 65] They are neither fully hydrophilic nor hydrophobic. Most water uptake occurs in the positive P_C range, indicating that force must be applied to inject water. Conversely, force must be applied to pull water out. Most of the uptake or removal happens in a narrow P_C range, which means that most pores are of a specific size and wettability. If not, we may have seen uptake or ejection occurring over a wider range of pressures or, in the more extreme case, we may have seen multiple plateaus for when one type of pore is filled and subsequently a second type of pore is filled, as may be seen in the case of a GDL with an MPL. The full cycling of a GDL can take place in the +/- 30 kPa range as seen by how the curve begins flattening on the injection side as we approach 30 kPa and again on the ejection side as we approach -30 kPa.

While the overall shape of the curves is fairly similar, we see characteristic signatures for some of the manufacturers. These signature features of each manufacturer's GDL is independent of PTFE loading. Therefore, the signatures are a result of the manufacturing process of the untreated GDLs. SEM images of the GDLs are discussed in a later section to observe what visually obvious differences, if any, exist between GDLs made by different manufacturers. Toray samples are distinguishable by a knee in the uptake portion of the curve near the zero-P_C line. Freudenberg samples show no residual saturation, indicating complete liquid withdrawal. This is particularly distinctive because most GDLs have 10 to 15% residual saturation due to stranded water. MRC samples show the greatest hysteretic difference between uptake and withdrawal, resulting in a wide curve. The MRC samples also require higher P_C than the other manufacturers' GDLs and demonstrate more hydrophobic character than GDLs that have been treated with PTFE.

We focus next on a single manufacturer to compare the effect of having different PTFE loadings. From this, we can see the effect of PTFE loading on the P_C-S curve and whether additional PTFE will make GDLs more hydrophobic. The secondary curves, curves taken subsequent to the initial wetting and withdrawal of the primary curve, are shown in Figure 2.7 for SGL 24 series GDLs at 0, 10, and 30% weight loading. On a cursory look, the untreated sample appears shifted more to the hydrophilic region, as may be expected because it does not have PTFE, and the other curves are less distinguishable from each other. A convenient means to assess neutrally wetting materials is by the US Bureau of Mines Index,

$$I_{USBM} = \log (A_{hydrophilic} / A_{hydrophobic}),$$

where A refers to the area of the curve in the hydrophilic or hydrophobic region of Pc. Hydrophilic materials will have a positive value whereas hydrophobic materials will have a negative value. Using this metric, the aforementioned curves for 0, 10, and 30% PTFE have indices of 0.58, -0.057, and -0.070, respectively. The addition of PTFE will shift a GDL from being hydrophilic to hydrophobic, but the extent of the PTFE loading, whether 10 or 30%, does not have as large of an effect. This trend is in line with findings from the literature in which is it seen that the initial addition of PTFE has the greatest effect,[66] and explains why PTFE in moderation is sufficient to improve performance.[67] This fact is useful when optimizing GDLs in

fuel cells because adding significantly more PTFE does not appreciably change wettability and may instead compromise electrical contact between the GDL and CL or current collectors.

Lastly, temperature and humidity effects were tested within the recommended temperature and humidity ranges for the syringe pump and balance, i.e., <40 C and <80% humidity. Temperature and humidity effects within the operational limits of the equipment were found to be negligible for the GDL. When the humidity was increased from ambient to 80% humidity at constant temperature, the evaporation rate decreased from 3.5×10^{-7} to 2.0×10^{-7}, but the curve was unchanged. Humidity is not expected to change the P_C-S measurements because it does not affect the interfacial properties between the water and GDL; the surface of the GDL is not altered unless water condenses on the fibers, at which point the experiment is compromised because saturation is not controlled. When temperature was increased from 25 to 40 C at constant humidity, the entire P_C-S curve shifted to the left by less than 1 kPa. As a point of reference, samples of the same type tested in the same conditions can vary by 2 kPa. If the temperature were high enough to decrease significantly the surface tension of water, we might expect to see the P_C-S curve to become thinner because less pressure would be required to invade or withdraw from a pore. Although 40 C does not appear to be a high enough temperature to cause this change, P_C-S curves should be tested at 60 to 80 C to confirm these results at temperatures that are closer to those used during fuel-cell operation.

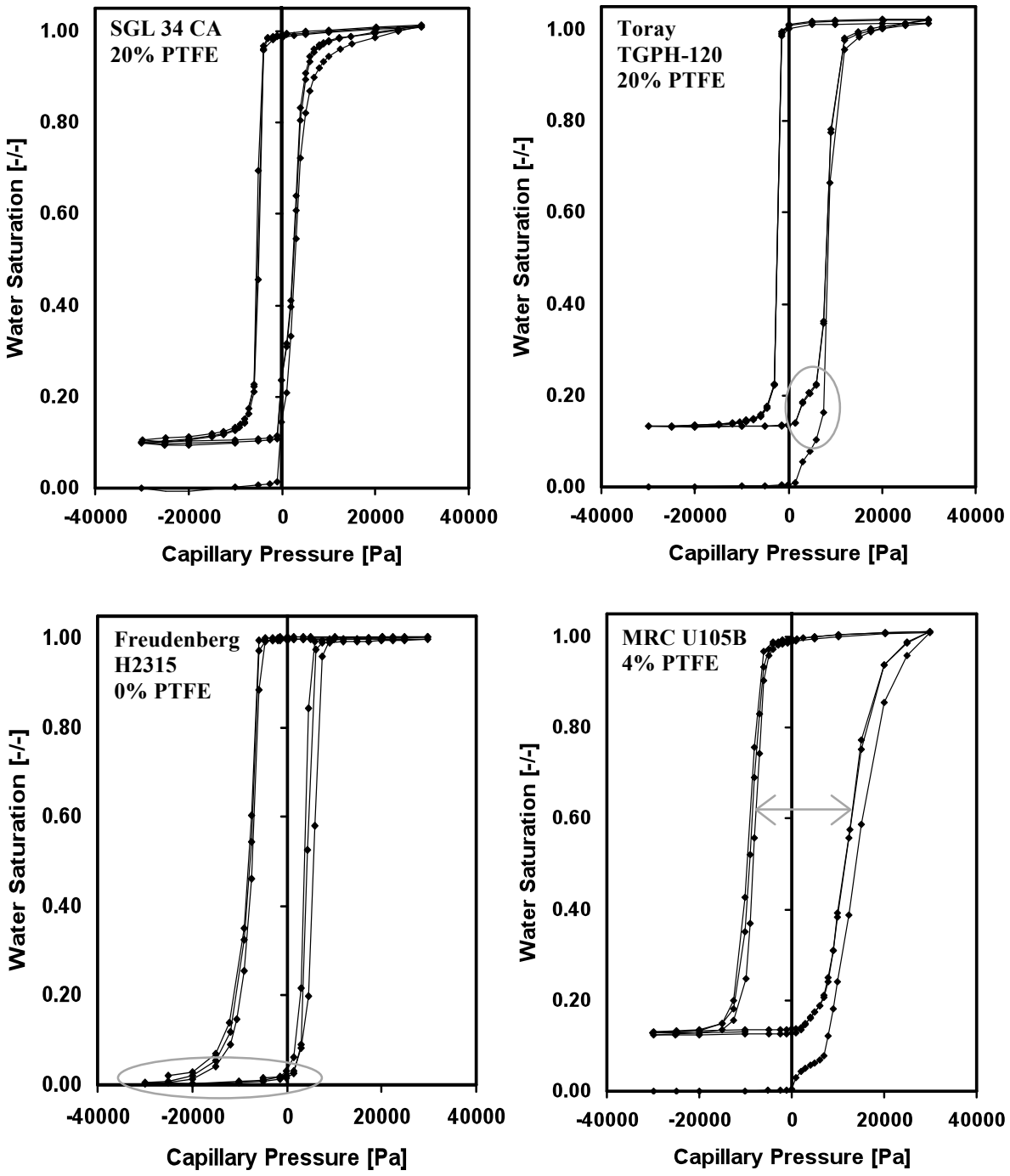

Figure 2.6. P_C-S curves for GDLs by SGL, Toray, Freudenberg, and MRC. Characteristic signatures of the GDLs are highlighted in grey. Toray samples show a knee in the uptake portion of the curve. Freudenberg samples show no residual saturation, indicating complete liquid withdrawal. MRC samples show the greatest hysteretic difference between uptake and withdrawal, resulting in a wide curve.

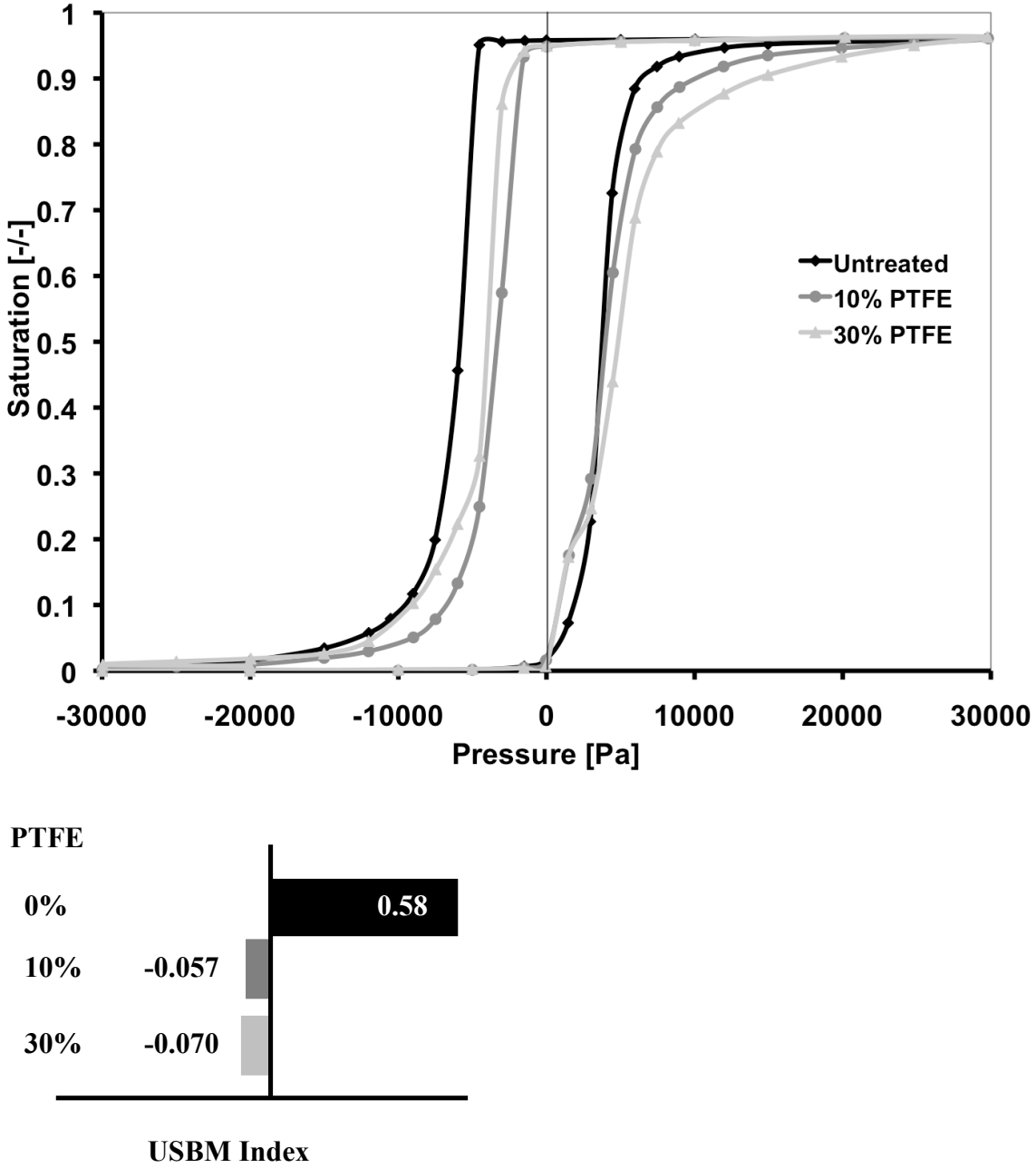

Figure 2.7. P_C-S secondary injection curves for SGL 24 series GDLs with corresponding US Bureau of Mines wettability index. The PTFE loadings used for comparison are from the 24 AA (untreated, 0% PTFE), 24 CA (10% PTFE), and 24 EA (30% PTFE).

2.3 P_C-S Curves of CLs

To date, there have been no data on the wettability and water-uptake behavior of CLs. P_C-S curves of CLs had not previously been studied because in addition to most attention for such measurements being given to GDLs, the CL typically is deposited onto the polymer-electrolyte membrane used in fuel cells and is not studied in isolation. To remedy this situation, an isolated CL was made by painting CL material directly onto hydrophobic PTFE membranes that are used in the measurement apparatus.

2.3.1 In-house CLs

20 wt% Pt/C (5:2 Pt/C:Nafion) CLs were made in-house according to the recipe developed at Los Alamos National Laboratory (LANL) and outlined in the Appendix. Using a paintbrush method, the ink was applied directly onto PTFE membranes from Sartorius Stedim with 0.2 μm pores. Successive layers of catalyst ink were added to the PTFE membranes and dried at 140°C between coatings. Coats were added until the catalyst layer began to show signs of cracking, which occurred typically around 20 to 40 μm. The samples were made to be as thick as possible given this limitation to increase available pore volume and facilitate accurate measurement. CL loading is given in terms of weight loading, with normal CLs being 0.1 to 0.2 mg Pt/cm^2. In contrast, the custom-made CLs have loadings as high as 0.8 mg Pt/cm^2. The thickness of the CLs was measured by profilometer. Each mg of catalyst material total (Pt, C, and binder) was found to correspond roughly to a 10 μm layer, although this estimate is imperfect. The paintbrush method inherently leads to an uneven distribution of the CL ink. A sample that is 30 μm thick will have portions of the layer ranging from 20 to 40 μm. Nonetheless, because most models characterize assorted layers according to thickness, we wished to define the CL by equivalent thickness. Classification by equivalent thickness will be useful when we discuss CLs made with different ink recipes. Images of CLs taken by scanning electron microscopy (SEM) are shown in Figure 2.8.

To prepare the sample before introduction into the measurement apparatus, the CL is brought to full saturation to establish an initial saturation level of 100%. This is in contrast to the traditional method of starting with a dry sample as discussed previously, because due to the water-wicking property of Nafion, a catalyst-layer measurement cannot be started from an initial saturation of zero. Once the catalyst layer comes into contact with the hydrophilic membrane and water reservoir, it takes up water. Instead, we aim for full saturation by preparing it in a similar fashion to the preparation of the hydrophilic membrane by placing the catalyst layer in a flask partially filled with water. The flask is evacuated by vacuum pump. Next, the water is tilted into contact with the catalyst layer so that water may wick into the sample and displace the air without entrapment. The sample is kept submerged in water as the vacuum is released and the sample is loaded onto the Pc-S measurement apparatus. The in-house CLs equilibrated quickly with water, and P_C-S results of CLs left in water for several days were the same as those obtained from CLs that were immediately transferred to the measurement apparatus. Capillary pressure is kept at zero or above to maintain saturation.

A P_C-S curve for a sodium-form Pt/C catalyst layer sample is shown in Figure 2.9a. Much of the curve lies in the negative P_C region and shows the highly hydrophilic nature of the CL. The withdrawal portion of the curve is observed by starting at the right and tracing the top curve toward the left. The withdrawal curve demonstrates little loss of saturation until P_G is greater than P_L and water begins to be ejected forcibly, not spontaneously. Water must be actively forced or drawn out of the CL. The curve shows a noticeable knee along the withdrawal curve that is a unique feature of the CL. The knee suggests an abundance of a type of pore, to be discussed, that leads to water ejection around -5 kPa. The trailing tail of the curve moving left shows that even at -80 kPa, all water is not removed from the catalyst layer. Subsequent injection of water shows a hysteretic effect and spontaneous imbibition occurring at capillary pressures as low as -30 kPa, which attests to the hydrophilicity of the catalyst layer. The path of the curves was also found to be reproducible when letting the system rest between cycles and restarting from high Pc.

Comparison of Figure 2.9a and 2.9b demonstrates the effect of the counterion in Nafion. Before use in fuel cells, the membrane-electrode assembly comprised of CL and Nafion is boiled in a sulfuric acid solution to exchange the sodium ions in Nafion for protons. Because the CL ink made for these experiments contains Nafion as a binder, both sodium and protonated forms of CLs were tested to establish the effect of the Nafion counterion. The protonated CL shown in 9b exhibits very similar characteristics to the sodium form with a small knee in the -5 kPa range and gradual uptake from -20 kPa through 0. Overall, protonation of the Nafion is seen to have minimal effect on the water uptake characteristics.

Next, we consider the effect of the catalyst particle composition on the P_C-S curve. Figure 2.9c depicts a P_C-S curve for a sodium sample made without Pt. The carbon-only sample shows more punctuated ejection and uptake phenomena near $P_C = 0$ as may be expected given the neutral-wetting behavior of carbon. We see by comparing Figures 2.9a and 2.9c that water movement in the -5 kPa to 0 range constitutes a larger proportion of the total water cycling profile for the carbon-only sample versus the Pt/C catalyst layer. The presence of Pt leads to a slower release of water on ejection and a more gradual uptake upon imbibition. The composition of the catalyst powder, Pt/C vs. C only, is seen to impose a greater effect on the shape of the P_C-S curve than does the composition of the polymer.

To explore further the effect of ink composition on water-uptake behavior, dynamic vapor sorption (DVS) was used to characterize the water-vapor sorption of the CLs as shown in Figure 2.10. Water content, λ, is calculated based on the fraction of ionomer present in the test sample according to the following equation:

$$\lambda_{catalyst} = \frac{M_{catalyst} - M_{catalyst}^{dry}}{f_{ionomer}(1-\varepsilon)M_{catalyst}^{dry}} \frac{EW}{18}$$

where M is the mass of the sample, $f_{ionomer}$ is the fraction of ionomer present in the CL, ε is the porosity, and EW is the equivalent weight of Nafion used, i.e. 1100 for our CLs. Typical λ values for Nafion range from 0 to 14. During DVS, the humidity is changed incrementally, and the sorption or desorption value is recorded.

A comparison of DVS measurements from a traditional Pt/C catalyst sample and one without Pt shows a higher water sorption curve in the presence of Pt. Differences in λ increase as relative humidity increases, thereby suggesting a compounding effect of Pt on water attraction; once a surface is wet, additional wetting is facilitated. Whether with or without Pt, the water content of the ionomer when mixed with catalyst powder is less than that of bulk ionomer in Nafion 117 across the entire humidity range. The increased propensity for water sorption by the Pt-containing sample is in agreement with the P_C-S curves discussed previously.

In summary, the results from the in-house CLs indicate that the Pt has a distinct wetting effect that leads to more gradual P_C-S profiles without distinct ejection or uptake events when compared to a carbon-only sample. The effect of the presence of Pt on water profiles is greater than the effect of protonation of the Nafion. Therefore the precious metal used in catalysts may play a dominant role in influencing P_C-S relations as opposed to other components of the catalyst layer, such as the ionomer.

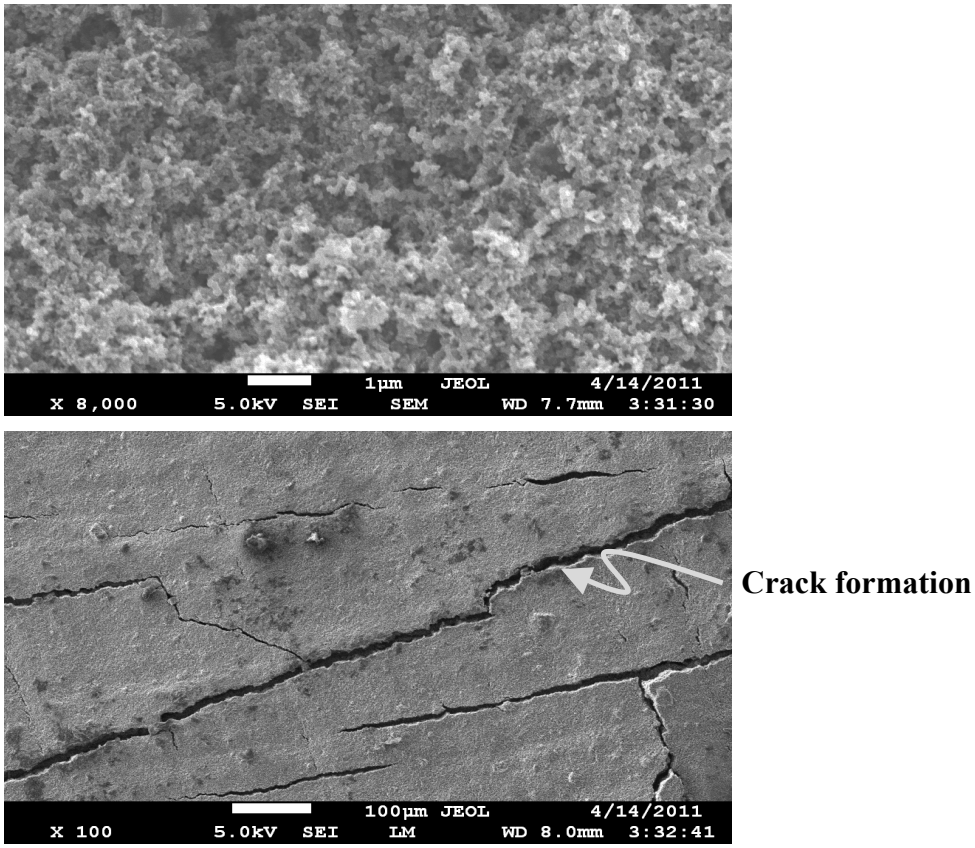

Figure 2.8. SEM of CL taken at 5 kV at different magnifications. The lower-magnification image shows the inevitable cracking that occurs when creating thick CLs. The extent of cracking can be mitigated by painting thinner layers and drying the layers more slowly at lower temperatures, but is difficult to control.

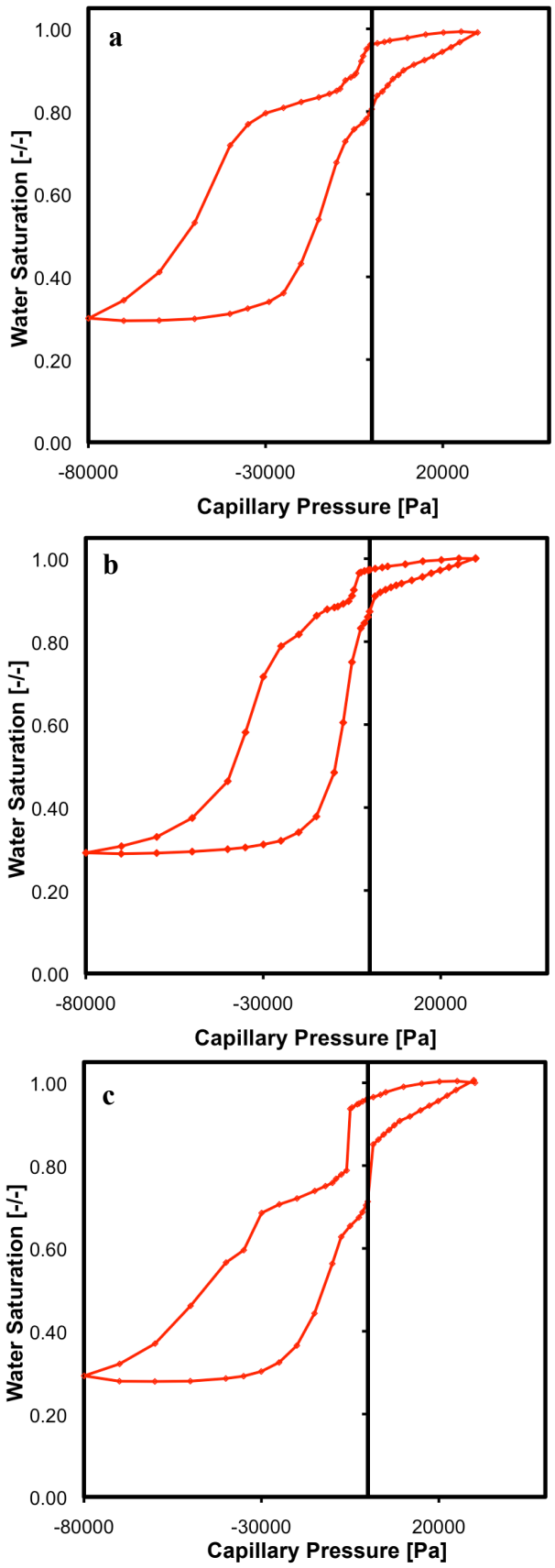

Figure 2.9.
Pc-S curves of 3 catalyst-layer samples. Runs are started at high capillary pressure and 100% saturation.

a) sample with 20 wt% Pt/C and 5:2 Pt/C:Nafion ratio for Nafion in sodium form.

b) Pt/C sample with Nafion in protonated form.

c) Sample without Pt, 2:1 C:Nafion ratio for Nafion in sodium form.

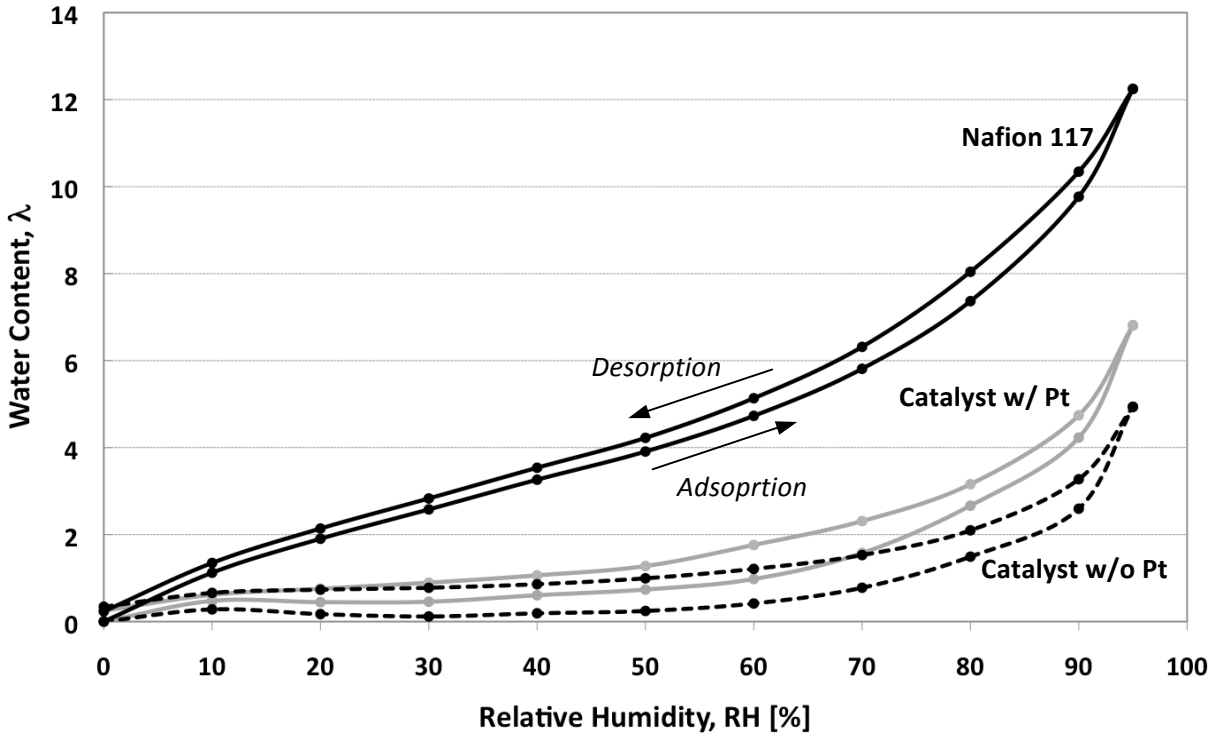

Figure 2.10. Water content as a function of humidity for bulk Nafion 117, catalyst-layer with 20wt% Pt/C and 5:2 Pt/C:Nafion, and catalyst layer with 2:1 C:Nafion. Nafion is in sodium form. Measurements were taken at 25 and 50 °C and yielded similar results. DVS data are courtesy of Ahmet Kusoglu.

2.3.2 Commercial CLs

Commercial CLs were obtained from Ion Power for P_C-S testing. All samples were made according to Ion Power's standard protocol that includes 25 wt% Pt/C catalyst and a 1:1 carbon to ionomer ratio, a departure from the LANL CLs which are made with 20 wt% Pt/C catalyst and 2:1 carbon to ionomer ratio. Contrary to the paint-brush method, the Ion Power ink is applied via an industrial-scale coating method in which the support membranes are sent through a printing device loaded with different inks. As can be seen from Table 2.1, commercial CL treatment still results in significant variation, e.g., samples with similar Pt loading may have thicknesses that vary by nearly 100%. The complexity is two-fold: first, the correlation between catalyst loading and thickness may be nonlinear due to changes in porosity with the addition of more ink. Second, determination of thickness by profilometer is challenging due to both physical and measurement variation between and within samples.

Table 2.1. Characteristics of commercial CL samples made by Ion Power. The main distinctions between samples are the thickness and surface appearance. Surface cracking occurs at greater thicknesses, and the presence of mudcrack-like formations is visible by eye. Inducing or preventing cracking systematically is difficult.

Sample	Thickness [μm]	Pt Loading: [mg/cm^2]	C:Ionomer	Surface
424A-1	10	0.12	1:1	Smooth
424A-2	19	0.15	1:1	Smooth
424B-1	58	0.27	1:1	Cracked

CLs from Ion Power are tested for the effects of thickness and cracking on wetting behavior. Results are shown in Figure 2.11 and indicate hydrophobic behavior for the smooth CLs with the majority of water uptake and ejection occurring in the positive P_C range. The thicker, 19 μm, sample shows uptake over a greater positive P_C region; this suggests greater pore-size and type variation as may be expected when compared to a thinner CL that may achieve more uniform composition. As thickness is increased from 19 to 58 μm, cracks form and would be expected to alter the pore-size distribution through the introduction of larger pores. The P_C-S curve widens further and also shows a marked shift in wettability from being more hydrophobic to hydrophilic. Whereas 50% saturation was once achieved at zero P_C, the thicker, cracked sample requires P_C below -20 kPa to achieve similar water ejection levels. The smoothed ejection profile in the negative-P_C region suggests not only greater variation in pore size but also that cracks may form preferentially with wetting surfaces.

Findings from these in-house and commercial CLs are the first of their kind that consider the water uptake characteristics of CLs specifically. Pt composition and presence of cracks are two key factors that can increase the hydrophilicity of a sample. Because morphology is thus far seen to cause the greatest shift in hydrophilicity, future studies of CLs should verify the effect of cracks that form when attempting to create thick samples for measurement purposes, or cracks due to normal use of CLs. Temperature and humidity effects should be studied for CLs, particularly for those with longer equilibration times than the in-house and Ion Power CLs.

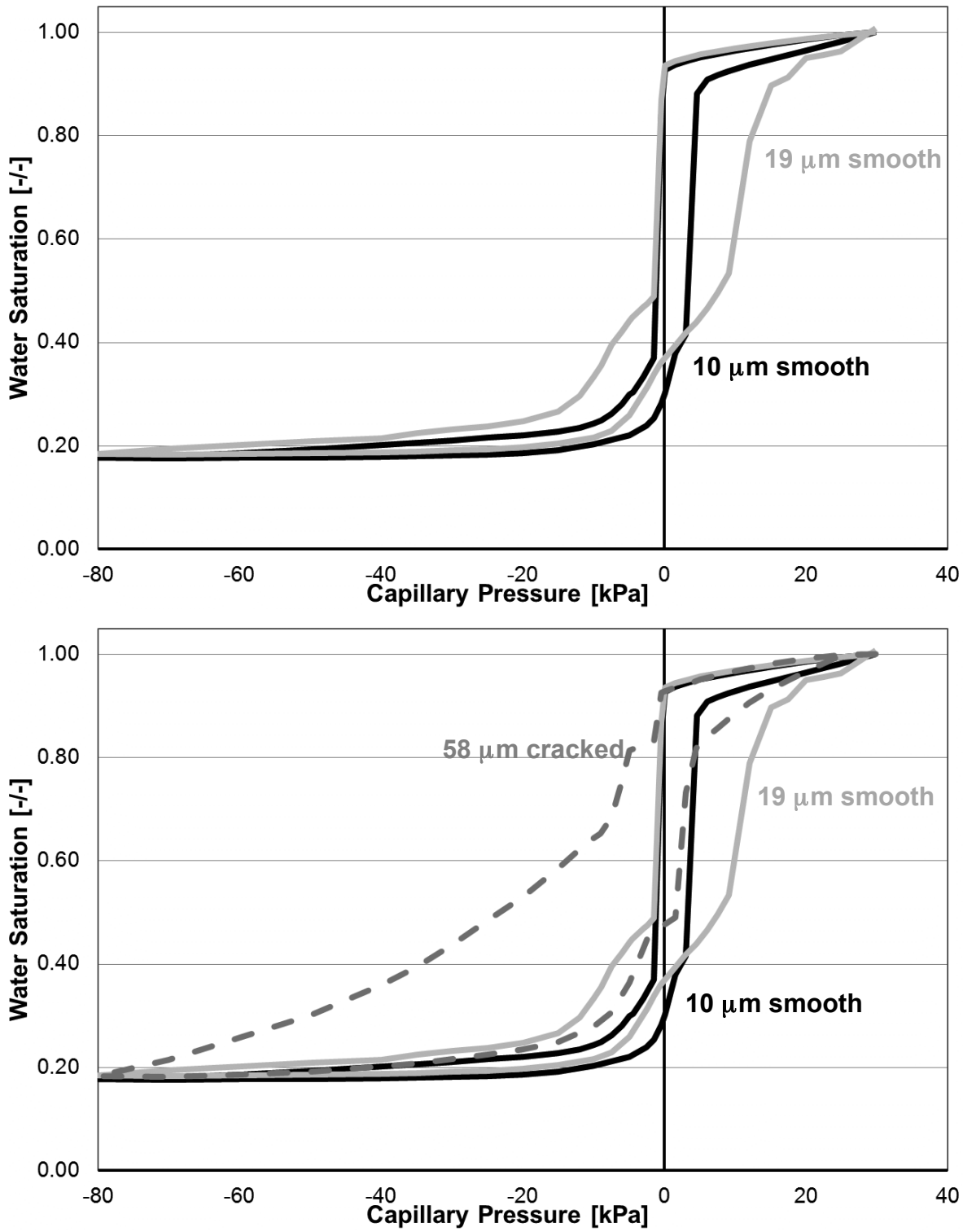

Figure 2.11. P_C-S curves for CLs from Ion Power. The bottom figure is identical to the top figure with one curve added. Tested samples vary in thickness and cracking. The porosity was estimated such that residual saturation was 20% to enable comparison of graph shapes.

Chapter 3.

3.1 Visual and Physical Characterizations

In addition to satisfying the natural curiosity for visualizing a material at hand, visual and physical characterizations of gas-diffusion layers (GDLs) are desirable first, to aid development of a physical intuition of results, and second, to identify variables that are key to simulations. Characterizations that can be incorporated directly, such as pore-size distributions (PSDs), are easily put to use. On a more nuanced level, there is no shortage of simulations and corresponding assumptions made to treat porous media. The characterizations provide a reality check for these assumptions and improve directed development by guiding the type and level of detail necessary. 2-D and 3-D visualizations of GDLs via scanning electron microscopy (SEM), energy dispersive X-ray (EDX), and synchrotron radiography are discussed. With regard to physical characterizations, mercury intrusion porosimetry (MIP) is used to collect and analyze PSD data.

3.2 Imaging Techniques

Many imaging studies have been conducted on GDLs through a variety of techniques.[68] Earlier works include light and fluorescence microscopy to observe droplet formation on the surface of GDLs. More elaborate studies include use of SEM and environmental SEM (ESEM) for nm resolution, neutron radiography that ascertains water location to within 100 μm resolution, or synchrotron radiography that has 10 μm resolution. Ideal visualization of the GDL would include the ability to capture the GDL's complex 3-D micrometer-level structure and nanometer surface variations, and doing so over a several-hundred micron scale in an environment conducive to liquid water. Meeting all these criteria is difficult. Imaging is therefore a tradeoff between resolution, field of view, timescale, and capability, e.g., the ability to examine conductive or saturated materials.

3.2.1 Scanning Electron Microscopy

SEM imaging is capable of nanometer resolution and functions by focusing an electron beam which raster scans the sample. The images that follow were obtained using a JEOL 7500F SEM machine operated at 5 keV. Figure 3.1 demonstrates the differences between untreated base materials as made by four GDL manufacturers: SGL, Toray, Freudenberg, and Mitubishi Rayon Corporation (MRC). Although the GDLs shown in Figure 3.1 are untreated, each particular binder used by several of the manufacturers leave excess material on the GDLs. This is particularly the case for the SGL sample that looks as though a heavy layer of dust has fallen upon a spider's web. The Toray sample shows patches of binder build-up along certain fibers, but unlike the rough SGL-binder surface, the Toray binder appears smoother and more shelf-like. Freudenberg has a very distinctive appearance of having clean annealing between fibers that twist and loop. Functionally, Freudenberg samples are also unique in that their capillary pressure versus saturation (P_C-S) curves do not show a residual saturation; all water is removed without any left stranded within the GDL. Based on the SEM images, the reason for this distinction could be imagined to be a combination of two factors: first, the clean structure of the Freudenberg GDL may not leave any shelves made by excess binder upon which water may sit and become stranded. Second, the curves and interconnectivity of fibers may serve as an improved scaffold over which water in different portions of the GDL may connect. In contrast to the Freudenberg binder that causes the least structural change, MRC's binder imparts a secondary pore structure. This additional structure corroborates the wide P_C-S curve of the MRC sample, which had suggested a wider distribution of pore types than present in other samples.

Images of the same four base samples treated with polytetrafluoroethylene (PTFE) coating are shown in Figure 3.2 and 3.3. Comparison of Figure 3.1 and 3.2 demonstrates how the PTFE tends to deposit in sheets or clumps on the GDLs. The PTFE treatment gives SGL a smoother look, while Toray and Freudenberg show sections of PTFE stretching between fibers. The SGL, Toray, and Freudenberg samples have been treated with 20% PTFE loading whereas the MRC PTFE sample is 4% PTFE, which may contribute to the near indistinguishability of the treated and untreated MRC sample. Higher-resolution images of SGL, Toray, and Freudenberg samples are shown in Figure 3.3. Here, the topography of the untreated sample is seen to affect where PTFE is deposited. The SGL sample, which had rough patches of binder on the fibers, shows some PTFE deposition on the fibers themselves, whereas for Toray and Freudenberg, the fibers are left predominantly unaffected. Untreated Toray has sheets of sintered binder that serves as a scaffold that supports wide regions of PTFE deposition between fibers. The cleanest annealed Freudenberg sample shows the least spread in PTFE deposition, e.g., PTFE is found only between fibers that lie next to each other. From different manufacturers come different fiber formations that cause or exacerbate differences in PTFE deposition. The variation could be due to several differences between the composition, manufacturing, or sintering process of the base material. Although details are not publicly disclosed, such differences in production may introduce compounding sources of variation.

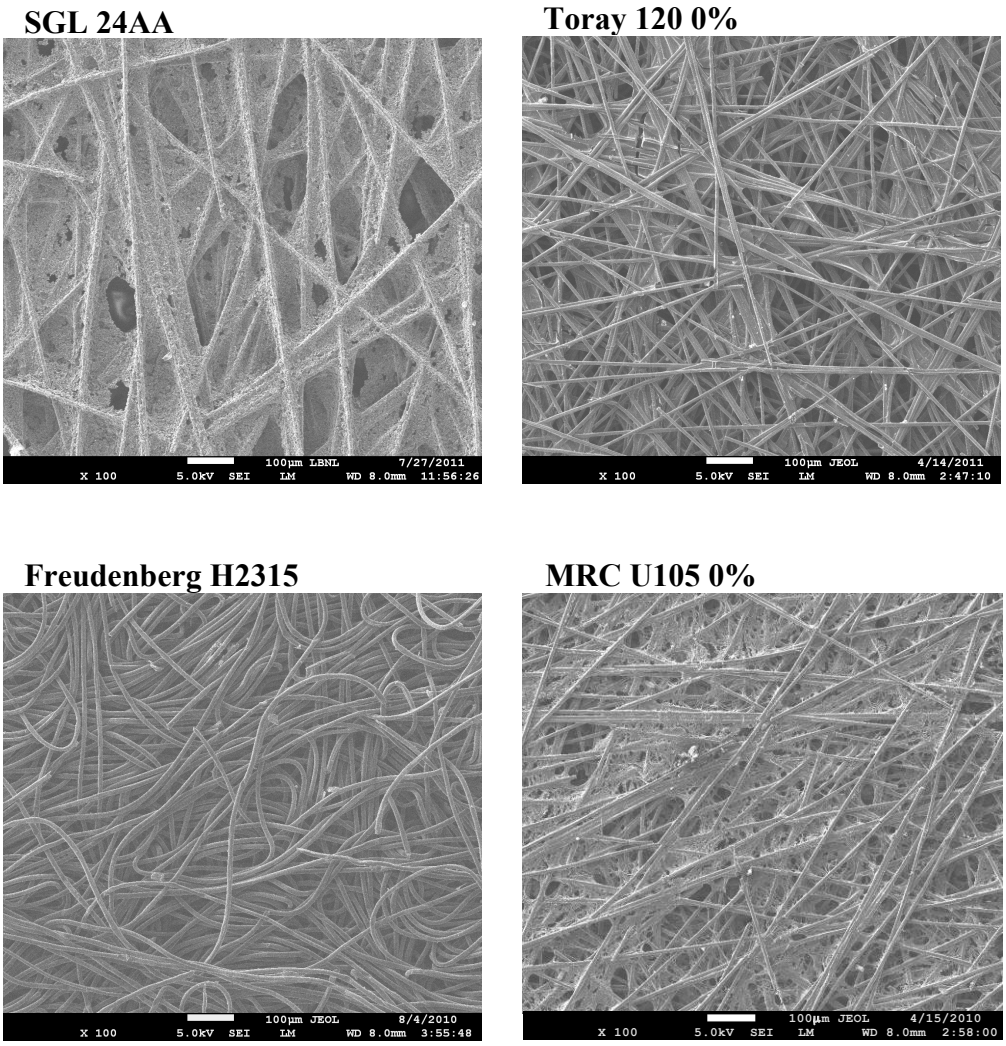

Figure 3.1. SEM images of untreated GDLs from SGL, Toray, Freudenberg, and MRC. The binder used by SGL, Toray, and MRC change the surface greatly. SGL's binder is roughest, Toray's deposits in sheets, and MRC's creates small surface openings in the PTFE. Freudenberg is unique both for the curved fibers and clean annealing between them.

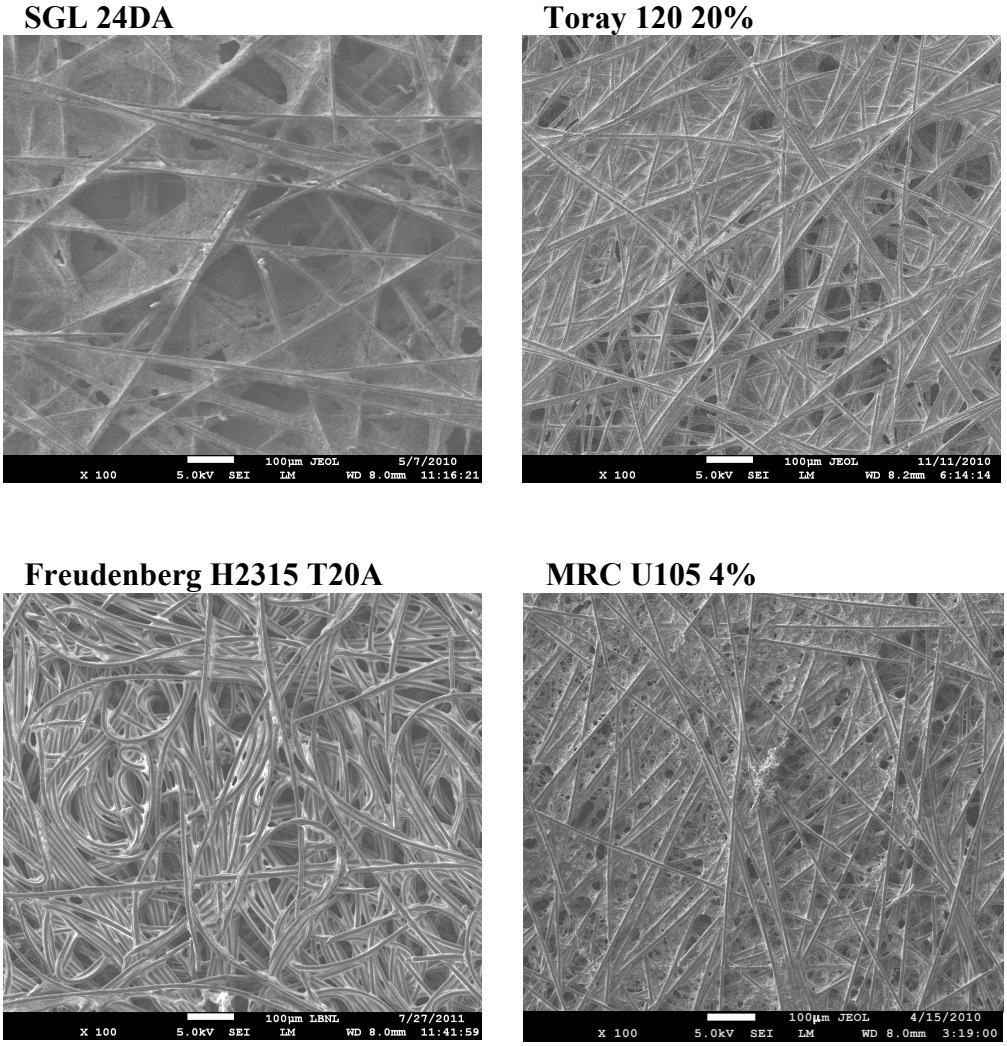

Figure 3.2. SEM images of GDLs from SGL, Toray, Freudenberg, and MRC. SGL, Toray, and Freudenberg are 20% PTFE, and the MRC sample is 4% PTFE. The brighter regions indicate PTFE deposition.

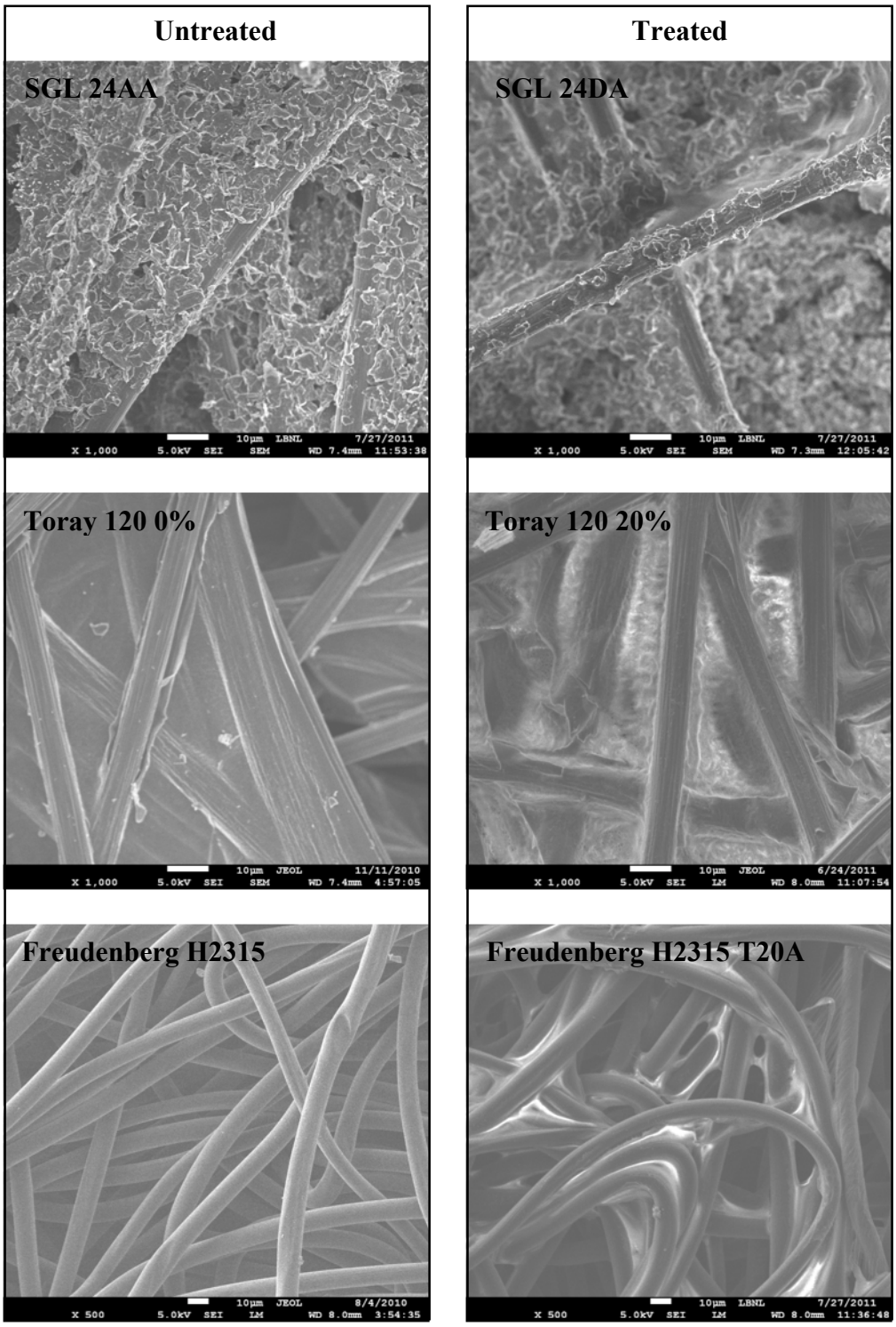

Figure 3.3. SEM images of SGL, Toray, and Freudenberg samples that are untreated (left) and treated with 20% PTFE (right). PTFE adheres differently to the GDLs depending on the underlying structure. For SGL and Toray, the PTFE adheres to the rough surfaces or shelves left by the binder. For Freudenberg, the PTFE deposits in small gaps between the fibers.

Lastly, Figure 3.4 depicts a progression of Toray samples as they are impregnated with increasing levels of PTFE. The initial PTFE coating adheres to the carbon fibers. As PTFE loading is increased, the fibers continue to be coated, but now successively larger pore regions are being filled with PTFE. This trend is in line with the observation from the P_C-S measurements that whether a sample is treated or untreated leads to a notable change in wettability, but there is little distinction between treated samples of different weight loadings. This trend is explained by the fact that PTFE coats the fibers first, thus covering the hydrophilic surfaces of the GDL. As more PTFE is added, the physical structure of the material is changed by the reduction of pore space, but the surface has already been altered from being wetting to nonwetting.

3.2.2 Energy Dispersive X-ray

EDX measurements of GDL cross sections were taken to observe the PTFE profile within GDLs. A through-plane observation is of interest because the PTFE deposition is measured in terms of a weight percentage, but the distribution of PTFE is not specified. EDX uses a bombardment of electrons to ascertain elemental fingerprints of the sample. When the incident beam displaces an electron from a lower shell, an electron from a higher shell drops and releases an X-ray. X-ray energies are unique for each atom and allow for elemental identification. For the purposes of identifying PTFE distribution, carbon and fluorine profiles were studied. The sample was prepared via freeze fracture. 2 to 3 mm strips of GDL were placed in liquid nitrogen and snapped apart with tweezers to expose internal surfaces. Samples are taped to an aluminum stage that has been cut away partially to allow samples to be mounted parallel to the detector's line of sight. Freeze fracture is preferred over traditional cutting techniques that crush the surface and cause fold-over of the MPL.

EDX results for an SGL 25BC sample (10% PTFE loading, 23% PTFE MPL) are shown in Figure 3.5. The carbon profile maintains uniform signal strength over the thickness of the GDL and indicates a fairly flat imaging surface that can be assessed by EDX. Comparison of the fluorine and carbon profile indicates that the fluorine, which should be using the carbon as a scaffold, is not evenly distributed. The increased levels of fluorine on the outer edge suggest that the PTFE coating is preferentially on the surface of the GDL, thereby creating chemical variation through the thickness of the GDL. This chemical variation means that without consideration of other phenomena occurring at the surface, water accumulation is more favorable in the center, more hydrophilic region, and less favorable on the outer, more hydrophobic, surface. Increasing PTFE levels would affect disproportionately the surface and compromise electrical contact between the GDL and catalyst layer or current collector. These and similar results from EDX measurements of other GDLs indicate that GDLs have significant nonuniformities in the through-plane direction. Physiochemical variation should be borne in mind in experimental and modeling contexts.

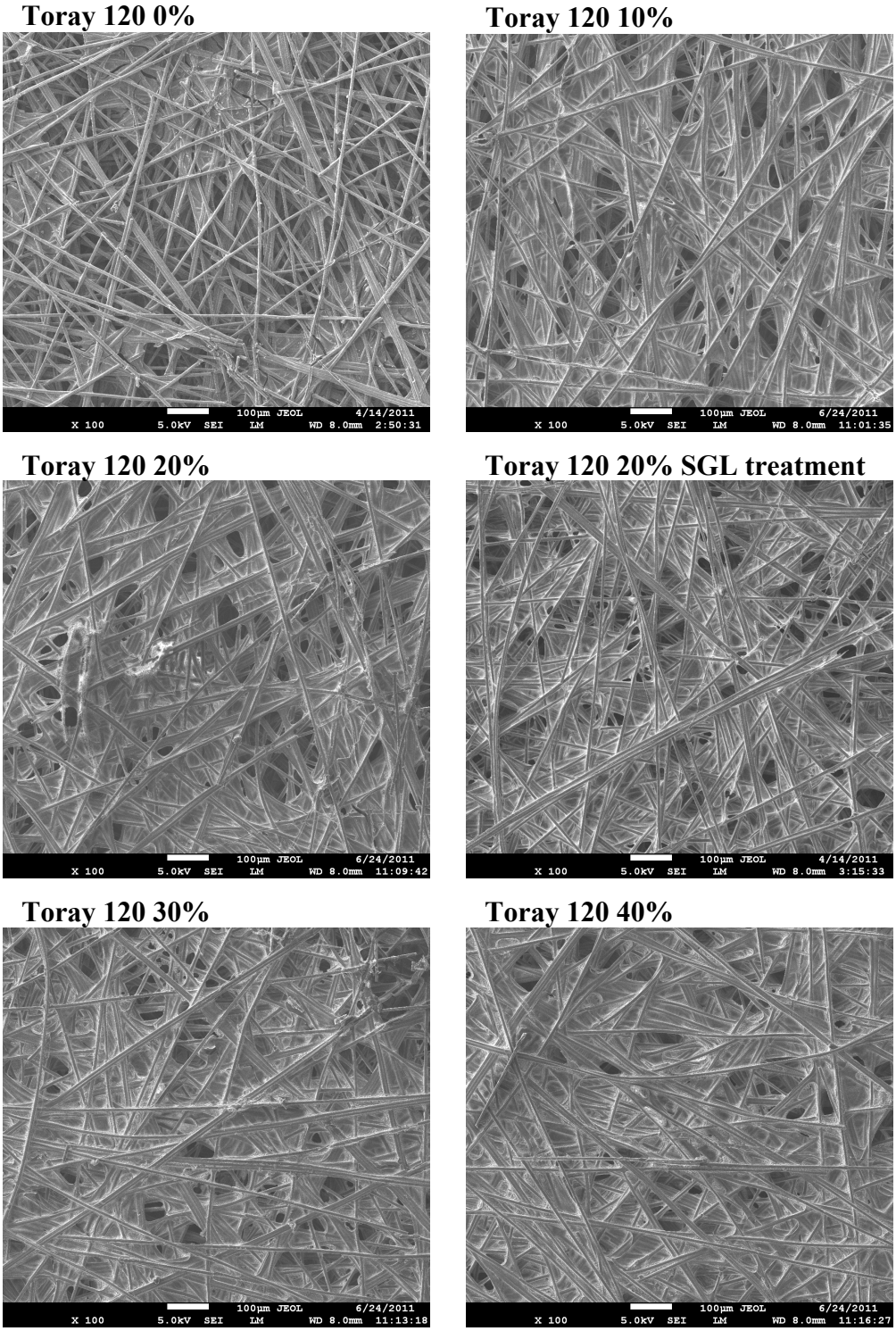

Figure 3.4. SEM images of Toray 120 GDLs with increasing levels of PTFE applied by Toray. A Toray raw substrate that was treated with PTFE by SGL is marked accordingly. Increasing PTFE loading from 10 to 30% does not lead to significant visual differences. The number of pores visible from the surface appears to decrease at 40% PTFE loading.

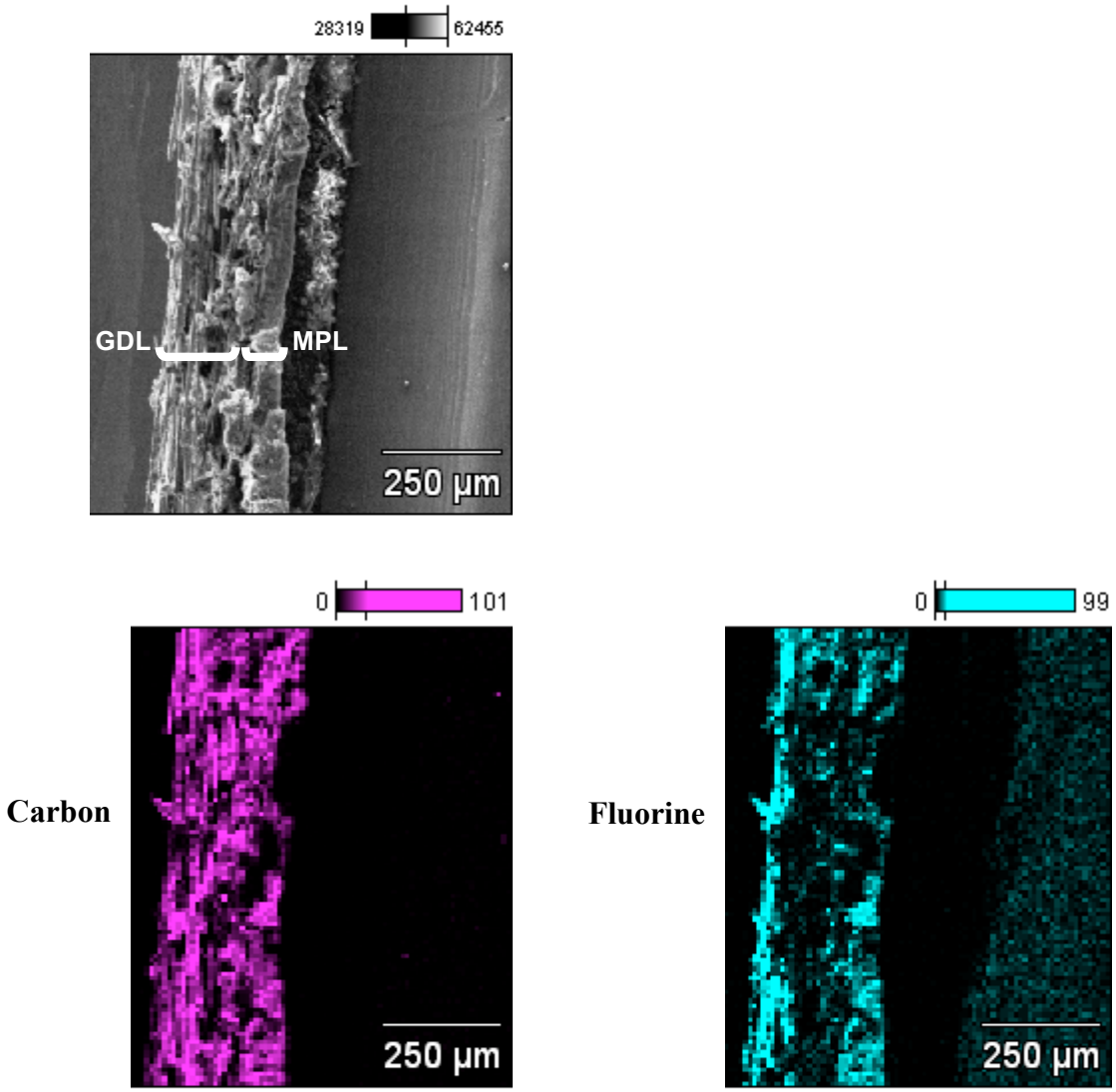

Figure 3.5. EDX images of SGL 25 BC. The top image is an SEM image of the cross section of the GDL and MPL. Below are the carbon and fluorine profiles. Whereas the carbon profile is fairly uniform over the thickness of the GDL, the fluorine profile shows preferential PTFE deposition on the surface despite the availability of a carbon fiber scaffold over the entire thickness. A nonuniform wettability is generated with the surface being more hydrophobic than the center.

3.2.3 Microtoming and SEM

The EDX through-plane images showed that physiochemical variation occurs through the thickness of the GDL. In order to get a better view of the cross-sectional slices, a sample is microtomed into layers by grinding the face of the GDL to isolate different strata. The SEM is employed again, this time to image the internal structure exposed via microtoming. Figure 3.6 shows successive 50 μm slices of GDL-H made by SGL. The total GDL is 350 μm thick and is ground to form 7 layers with the 4th layer being in the center. Figure 3.6 shows 4 of the 7 layers, going from the outside in, with the remaining slices being similar about the center plane of symmetry. The level of PTFE impregnation drops significantly when comparing the outer slices to the innermost 50 μm slice. This observation coincides with the EDX results in which PTFE was found to be deposited primarily along the surface. SEM resolution is higher than EDX resolution, and from these clearer images, the maximum PTFE deposition is seen to occur 50 to 100 μm below the surface. Water may be more likely to pool in the sparsely coated middle region. This coincides with neutron imaging results from Weber and Hickner that show liquid hold-up to be more likely to occur in the middle region of the cathode-side GDL.[69] The combination of pore structure and wettability variation through the thickness of the GDL should therefore be included in saturation simulations to capture the interplay between physiochemical effects and liquid buildup.

3.2.4 Focused Ion-Beam Scanning Electron Microscopy

One last 2-D imaging technique is mentioned for point of reference: focused ion-beam scanning electron microscopy (FIB-SEM, hereafter referred to as FIB). FIB is a destructive process that etches the sample surface with gallium ions while taking SEM images. These successive scans can then be reconstructed to create a 3-D visualization. This technique has been used successfully for analyzing domains in composite materials, including a solid-oxide fuel-cell anode.[70-72] Because SEM has nanometer-scale resolution, the resulting image would be clear enough to discern the difference between fiber, PTFE, and void. However, the GDL is too hard to allow ablation in a reasonable amount of time, e.g., a 10 by 10 μm^2 patch is only very faintly etched after 5 minutes of ion bombardment. As such, although physical microtoming coupled with SEM cannot deliver 3-D reconstructions, it is a more fruitful way to image internal structure than attempting to etch and image a GDL with FIB.

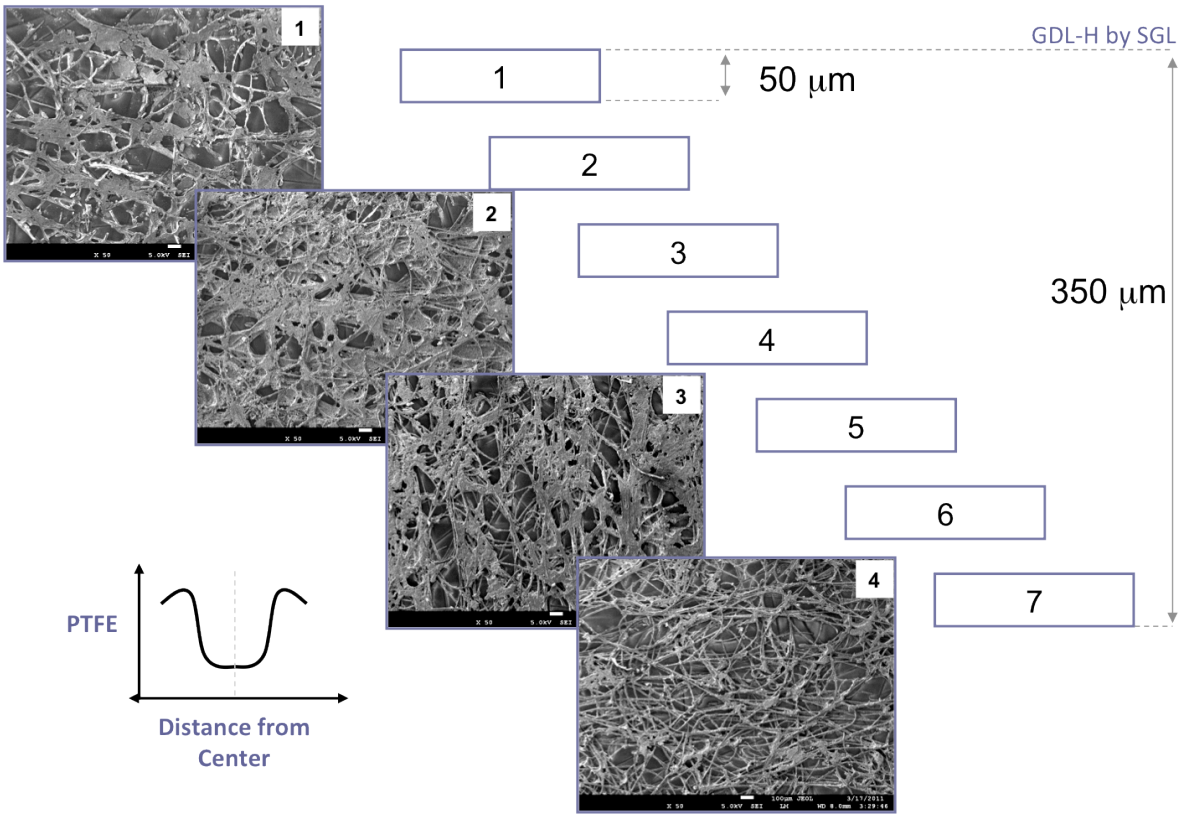

Figure 3.6. SEM images of a GDL-H sample made by SGL and microtomed by Karren More at Oak Ridge National Laboratory. The 350 μm GDL was microtomed into 7 layers, and images of the first 4 layers moving from the outside in are shown. A qualitative illustration depicting the level of PTFE in the sample as a function of the distance from the center is included.

3.2.5 Synchrotron Radiography

While the previously discussed techniques have provided 2-D images, synchrotron radiography is promising as a means to obtain 3-D characterizations of GDL in a dry or wet state.[31, 73-76] Of the typical techniques used for water imaging—neutron radiography,[69, 77, 78] magnetic resonance imaging,[79, 80] and synchrotron radiography[81, 82]—synchrotron radiography is the only option with both sufficient resolution and capability to visualize conductive materials. Synchrotron radiography employs an electron accelerator to generate a high-intensity X-ray beam. The beam is focused through a crystal monochromator onto an object of interest. The X-rays are absorbed by the sample or transmitted, and impinge upon a scintillator that fluoresces in the visible light range. The resulting signal is detected by a charge-coupled device and output for data reconstruction. A 3-D tomographic image is obtained by taking images while rotating the sample through a series of angles. The individual image slices are reconstructed to form one cohesive 3-D rendering.

Currently, effective resolution for tomography is on the order of 10 μm when applied to a fuel-cell system. Ongoing challenges with regard to imaging GDLs and water include the high porosity, similarity of electron density between the elements present—carbon, fluorine, nitrogen, oxygen—and the overall weak absorption properties. These factors complicate phase parsing for GDLs. Although the eye can distinguish between fibers, void, and water, computerized identification and quantitative analysis are challenging due to the narrow grayscale between signals and the inherent noise due to beam fluctuations. Nonetheless, progress continues to be made in both technique optimization and equipment capabilities, e.g., improved monochromater and camera quality. The work that follows was done at the Advanced Light Source at Lawrence Berkeley National Laboratory. The X-rays are provided by a 1.9 GeV superbend magnet, and the particular beamline used can be tuned to deliver X-rays in the 6 to 46 keV range.

A dry GDL from E-tek was exposed to a 14 keV electron beam and tested to determine optimal operation parameters, e.g., beam strength, imaging method, and contrast additive. Beam strengths in the 10 to 25 keV range provided the best data. Next, two imaging methods were tested: absorption contrast and phase contrast. The absorption contrast method utilizes differences in X-ray transmission levels to distinguish between different materials. Transmission levels vary according to the material thickness and absorption coefficient at a given energy and follow Beer-Lambert's law, i.e., thicker or more absorptive materials transmit less signal. The phase-contrast technique uses coherence phenomena and processes phase shifts in signal due to signal waves combining constructively or destructively. Phase contrast has the advantage that it enhances edges and makes boundaries easier to see, but the exposure time is longer because this method requires higher transmission to capture enough signal from the interference patterns.[83] Phase contrast worked to an extent for the GDL, but the presence of too many edges from the fine fibers made edge separation difficult, or would require downsizing significantly the imaged area. Absorption contrast was selected for these reasons. In order to improve the absorptive contrast of the GDL, the effects of a contrast additive were investigated. The GDL was filled with a potassium-iodide salt solution. Iodine is more electron dense and is easy to distinguish from the transmission signal of carbon. However, the results did not show a significant improvement. The iodine signal was overpowering at the higher energy level because the higher

beam strength also led to high transmission through the carbon fibers. At lower energies, where carbon can be imaged, the advantage of using iodide was negated. Fluckiger et al.[75] suggest that this is because the low energy, in their case, 10 keV, is too far below iodine's X-ray emission energy of 33 keV to yield a difference in signal. The GDLs were therefore visualized using the absorption contrast method without a contrast additive.

Resulting images were processed to remove artifacts and rendered in three dimensions using reconstruction software. Tomographic rendering for the dry E-tek carbon paper sample is shown in Figure 3.7. Figure 3.7 suggests that surface densification may be occurring in the GDL, possibly caused by the method by which carbon fibers are pressed together or how the PTFE is deposited nonuniformly. Identifying density variations is important because, as seen from SEM images, the structure of the fibrous carbon scaffold alters where and how PTFE may adhere to the GDL. Changes to the contact angle are of particular concern because from a theoretical basis, the contact angle is the main factor that determines whether a pore will be filled. According to the Young-Laplace equation, the contact-angle term switches the sign of P_C at which a liquid may enter a pore of a certain radius. Results from these 2-D and 3-D single-phase images suggest that GDL simulations should not assume uniform porosity and PTFE distributions in the through-plane direction, but rather divide the GDL into three or more regions to capture more accurately physiochemical variations.

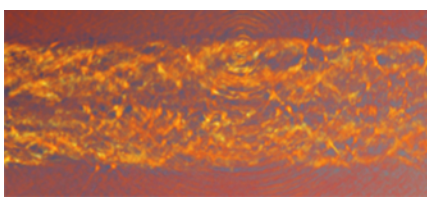

Figure 3.7. E-tek carbon paper imaged at 14 keV and showing some surface densification. Ring artifacts and signal noise from the surrounding air are present after attempts to filter extraneous signal while still preserving data from the GDL.

Lastly, synchrotron radiography is used to image GDLs with water. Improvements in beam intensity, monochromator, camera, and reconstruction software have increased image clarity to enable phase parsing by eye. If the GDL is hydrophobic, the water is expected to fill the space enclosed by fibers as an inscribed circle, as shown in Figure 3.8a. If the GDL is hydrophilic, water will preferentially wet the fibers, resulting in a more angular formation (Figure 3.8b). A Toray 120 sample with 20% PTFE was loaded in a custom-made, water-tight aluminum holder developed by Gostick.[84] The sample is held in place by sandwiching it between a hydrophilic and hydrophobic plug, and water pressure is controlled via hydrostatic head by connecting a tube to the hydrophilic side. The GDL was first imaged dry, then held at a P_C of 6 kPa for 20 minutes to ensure steady-state saturation. The files were reconstructed according to the back-projection algorithm used by Buchi and colleagues.[75, 83, 85, 86] In-plane slices taken from the GDL in a dry and partially-saturated state are shown in Figure 3.9. Darker regions correspond to void, and lighter areas correspond to fibers and water. The wet image matches the expectation set by the corresponding P_C-S diagram that demonstrates a saturation level near 40% at 6 kPa for this sample. The water takes on a rounded shape enclosed by fibers, as would be expected for an initial imbibition and penetration into a hydrophobic material. A similar image, not pictured, from a sample undergoing liquid withdrawal shows water clinging

along the fibers, maximizing surface contact. This observation is in line with the finding from P_C-S curves that GDLs behave hydrophobically during injection and hydrophilically during withdrawal.[64-66] The images thus confirm that hysteresis is important in determining the wettability of the GDL and the contact angle of the GDL-water interface.

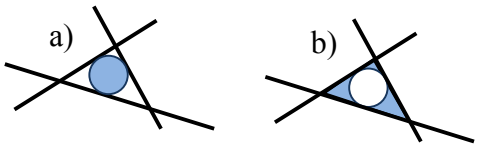

Figure 3.8. a) Illustration of water inside an area enclosed by hydrophobic surfaces. Contact with the fibers is minimized in this inscribed-circle formation.
b) Illustration of water inside a hydrophilic area. The water-fiber contact angle is below 90°, and contact with the fibers is maximized, resulting in a more angular appearance.

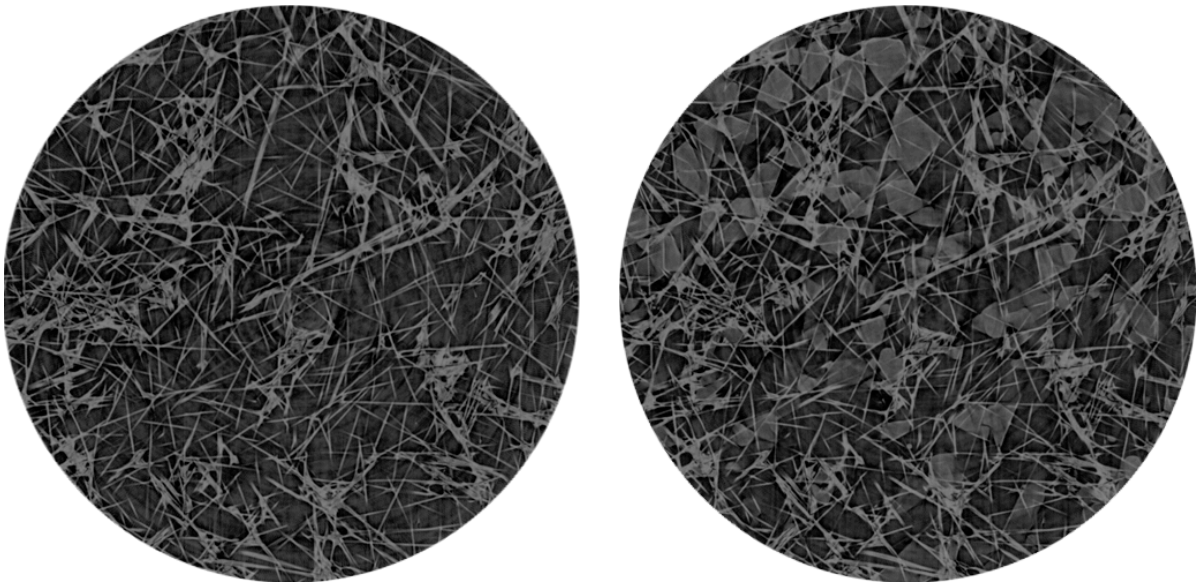

Figure 3.9. In-plane image of Toray 120 20% PTFE in dry (left) and wet (right) conditions. A P_C of 6 kPa was applied to the wet sample. The fibers are identified by their straight lines, and the water is seen to fill the voids in rounded cross-sections. Images are courtesy of Jeff Gostick.

3.3 Physical Characterization

3.3.1 Pore-size Distribution

A fundamental physical characterization for porous media is the pore-size distribution (PSD). Most porous materials are polydisperse to some degree; a PSD provides an intuitive understanding of the material by describing the pores as cylinders of a certain radius. The PSD is found by mercury intrusion porosimetry (MIP), a technique used on porous materials to determine pore size, volume, and surface area. In MIP, a sample is immersed in mercury, and pressure is slowly increased to force mercury to enter the pores. This measured intrusion volume, in conjunction with the pressure at which it occurred, and the contact angle and surface tension of mercury, is used to calculate the pore radius according to the Young-Laplace equation. MIP is a destructive process due to the use of mercury and also any damage wrought by probing high pressures. PSDs of GDLs can be input directly into simulations to predict water entry into the pores, or be used as empirical data to fit a mathematical expression, such as a Gaussian or log-normal distribution, to reduce the PSD into tractable parameters that facilitate analytic treatment. An analytic contact angle distribution can be found by using the PSD and experimentally determined P_C-S curve. The resulting mathematically described, continuous distributions are used to characterize and analyze a medium that is otherwise highly nonideal in structure and heterogeneous in surface wetting properties.

Although a fundamental piece of information for further porous-media analysis, PSDs for GDLs can be difficult to amass due to the need for specialized equipment, use of mercury, and time intensity. As of 2011, commercial testing services charge upwards of $200 per sample for a basic PSD measurement, and one can easily spend $300 per sample with the inclusion of a handful of additional tests, e.g., bulk density and hysteresis measurements. Parametric studies of GDL PSDs are hence rare, and distinguishing between effects due to basic inputs, such as manufacturer or PTFE loading, are difficult. To alleviate the paucity of available data and help isolate different effects, a collection of PSDs were obtained both in-house and commercially. Variables include manufacturer, PTFE loading, thickness, MPL presence, MPL penetration, catalyst layer, and testing reproducibility.

The effects of PTFE loading and the manufacturer are elaborated. An example of MIP data and a table of selected results are shown in Figure 3.10 and Table 3.1, respectively. GDLs made and treated by Toray with PTFE loadings from 0 to 60% show that structurally, the addition of PTFE up to 50% does not significantly alter or shift the PSD; PTFE is not preferentially depositing on smaller or larger pores in the Toray GDL. The 60% results depart from the steady trend and when tested, both privately by the author and commercially, the 60% median pore size departs drastically from the 0 to 50% results. The porosity trends provide an explanation: the porosity decreases steadily as PTFE is increased to 50%, and then drops drastically at 60% weight loading. This suggests that past a critical weight loading, PTFE is abundant enough to create dead volume in the GDL, i.e., the PTFE connects and isolates sections of the GDL so that fluid cannot enter. This would decrease the porosity dramatically, as seen here, and also increase variability in PSD; the effective pore size can be imagined to be dependent on how the PTFE intraconnects and which pathways it blocks.

Next, the effect of which manufacturer applies PTFE is studied through a comparison of a Toray sample treated by Toray and the same series treated by SGL. SGL's 20% PTFE treatment yields similar results to Toray's 20% PTFE treatment. Between SGL and Toray, any differences in the PTFE application process are negligible. However, comparison of Toray 0 and 20% samples with SGL10 or SGL24 0 and 20% samples demonstrate that PTFE loading can have a large effect depending on the underlying structure. The Toray PTFE PSD results are independent of loading, but the SGL results are not. The median pore size of SGL samples increases with the addition of PTFE; the smaller pores appear to be filling with PTFE, thus causing an upward shift in pore size. The base structure of SGL must vary from Toray in a way that causes a change in PTFE deposition, because who applies the PTFE is not a source of variation.

Lastly, the intra- and inter-product variability of SGL GDLs is probed by testing two samples of the same type, followed by samples of different types. The SGL10 series are 415 μm thick whereas the SGL24 series are 190 μm. The SGL 10AA, GDL with no PTFE, was tested twice and yielded median pore diameters that differed by 10 μm which, for scale of reference, is greater than the variation between the 0 to 50% PTFE Toray samples which was at most 3 μm. Because the intra-product variability is high, data for GDLs made by SGLs are assessed qualitatively rather than quantitatively. In a comparison of samples of different type, the thicker samples, 10 series, show a higher median pore volume than the thinner samples, 24 series, both in untreated and treated states, e.g., 10AA > 24AA and 10DA > 24DA. One explanation for this trend could be that the thicker a sample, the more degrees of freedom exist for how pores connect, and therefore the apparent pore size will increase. Overall, the SGL samples exhibit far less uniformity than the Toray samples, and these differences can cause greater fluctuations in PSD as the GDL is further processed. The high degree of variation between SGL samples of the same type would need to be better characterized before drawing absolute conclusions.

Although expensive to obtain, the PSDs of Toray and SGL GDLs demonstrate that more systematic, parametric studies of GDLs are necessary to enable accurate quantification of PSD characteristics. Preliminary results elucidate that the manufacturer of the basic, untreated, material is a major determinant in the uniformity of samples. Nonuniformities can then be compounded with the addition of PTFE and preferential deposition of the PTFE in certain pores and configurations. If the base material is reasonably uniform, as is the case for the Toray TGPH120 series, increasing PTFE loading will steadily decrease porosity until a critical amount of PTFE is introduced. When PTFE is over 50 wt%, the PTFE may enclose space and create dead volume, thereby drastically reducing measured porosity. If the base material is nonuniform, as is the case for SGL, increasing PTFE loading or sample thickness can shift the PSD toward larger pores.

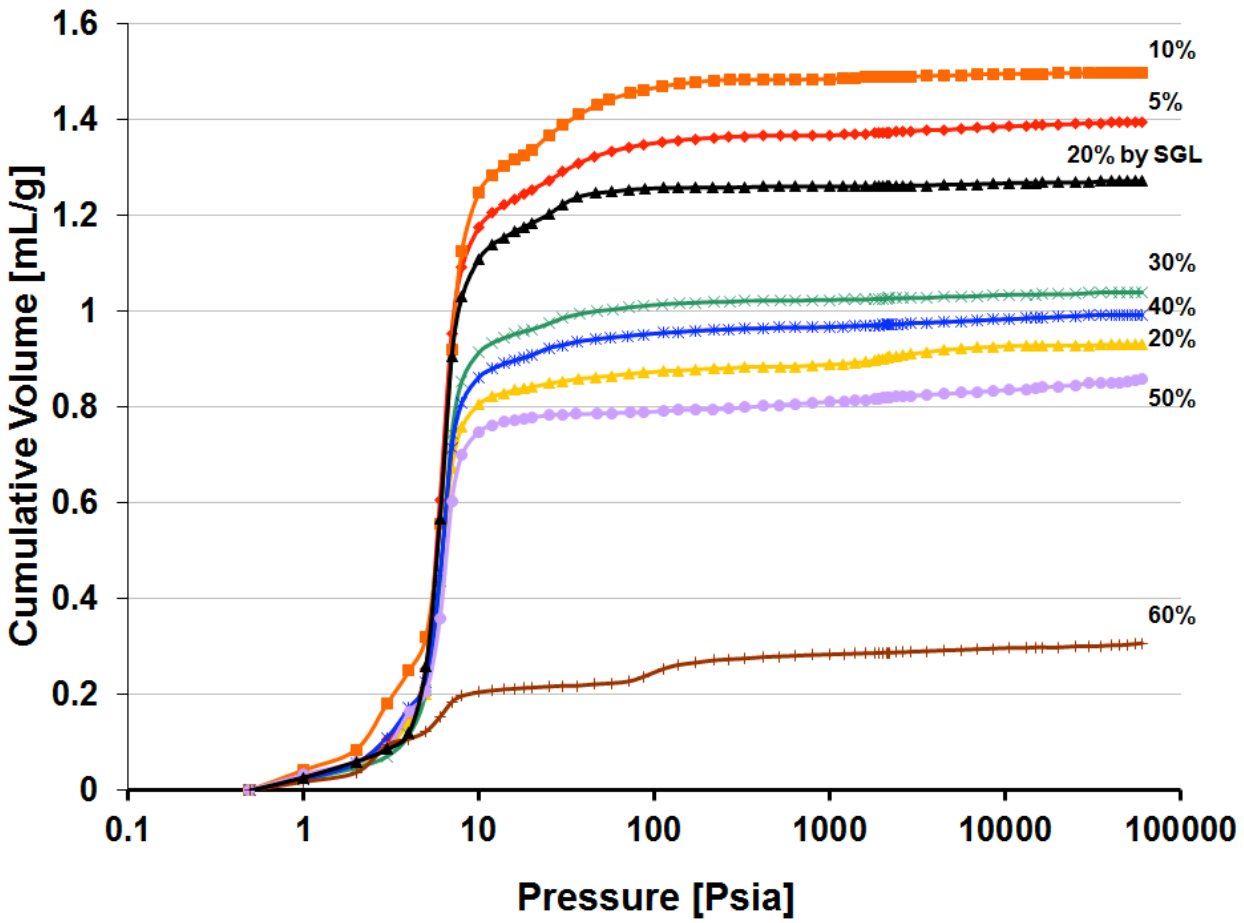

Figure 3.10. MIP data for Toray TGPH120 samples that range in PTFE loadings from 0 to 60%. The basic output is the cumulative mercury-intrusion volume at different mercury pressures. The surface tension of mercury and contact angle, which is constant for all materials, can be used in conjunction with the Young-Laplace equation to generate data that demonstrates the volume contribution of each pore size. The pressure at which the majority of uptake occurs, near 4 psia (0.3 bar), is similar for all the samples and indicates a fairly tight PSD; if the PSD were varied, the cumulative volume would climb steadily rather than rise sharply. A quick look at the raw data also suggests that increasing levels of PTFE loading causes step changes, and the effect on porosity can be classified loosely into 3 PTFE loading regions: <20%, 20 to 50%, and >50%. A more detailed look at the data shows that the greatest loss in porosity occurs when PTFE loading is pushed to 60%,

Table 3.1 MIP results for GDLs made by Toray and SGL and treated with PTFE. All samples are with the GDL only, no MPL. The manufacturer of the plain GDL and the company that applied the PTFE is specified as is the PTFE wt% applied. "Testing agent" refers to whether the tests were run by an external company or run by the author with an MIP device at Los Alamos National Laboratory. The effect of PTFE loading is studied for Toray GDLs that are treated with PTFE by Toray. A custom sample, a Toray GDL that was treated with PTFE by SGL, is also tested to check for variation due to PTFE applicator. Reproducibility is tested with the SGL 10, 0% PTFE loading by comparing results from the same company. Variation between different product series by the same manufacturer is demonstrated through a comparison of the SGL 10 and 24 series. The raw MIP data are included in the Appendix, as are data for more GDLs: those with standard MPLs, those with MPLs that penetrate into the GDL, and those that have been subjected to extreme freeze-thaw cycles. The median pore diameter is by volume. Privately tested samples were roughly 2 cm^2, and commercially tested samples were roughly 4 cm^2.

Product name	Manufacturer: untreated GDL	Manufacturer: PTFE application	PTFE [wt%]	Testing agent	Median diameter [μm]	Porosity
TGPH-120	Toray	Toray	0	commercial	28.165	-
TGPH-120	Toray	Toray	5	private	28.951	73.073
TGPH-120	Toray	Toray	10	private	27.784	72.761
TGPH-120	Toray	Toray	20	private	29.606	64.795
TGPH-120	Toray	Toray	30	private	28.858	63.469
TGPH-120	Toray	Toray	40	private	29.370	63.249
TGPH-120	Toray	Toray	50	private	28.766	58.719
TGPH-120	Toray	Toray	60	private	30.120	27.331
TGPH-120	Toray	Toray	60	commercial	39.948	-
TGPH-120	Toray	SGL	20	private	29.204	63.736
SGL 10AA	SGL	SGL	0	commercial	74.188	-
SGL 10AA	SGL	SGL	0	commercial	65.613	-
SGL 10DA	SGL	SGL	20	commercial	74.515	-
SGL 24AA	SGL	SGL	0	commercial	29.580	-
SGL 24DA	SGL	SGL	20	commercial	54.750	-

Chapter 4.

4.1 Effective-Diffusion Measurements

Ultimately, liquid build-up in fuel cells is a concern in so far as it obstructs gas flow. The end goal of saturation studies of fuel-cell materials is experimental determination of gas diffusion as a function of countercurrent water flow or saturation. Typical governing equations used in macrohomogeneous models include Darcy's law[17] and Stefan-Maxwell multicomponent transport.[18] Accurate implementation of these relations requires knowledge of the effective transport properties, such as permeability or diffusivity, which are unknown for fuel-cell diffusion media (DM), especially under operation. The DM are further composed of two distinct layers, a gas-diffusion layer (GDL) and a microporous layer (MPL), with different transport properties. For lack of information, many simulations that include two-phase effects on transport in fuel cells estimate saturation-dependent diffusion with constitutive relations similar to that of the Bruggeman,[41] Wyllie,[17] Corey,[42] Brooks-Cory,[87] or Van Genuchten[44] expressions. Saturation effects are commonly included in simulations as a multiplier in front of the diffusive term as $(1-S)^n$, where S is saturation and n is an integer or fraction. Thus far, the only experimental means to incorporate saturation into simulations is through the capillary pressure versus saturation (P_C-S) measurement; P_C is used to determine saturation, and saturation is used to estimate transport parameters. While these curves are useful, a more direct route is to run in-situ experiments and determine how saturation affects gas diffusion. There exists a desire for dynamic measurement of countercurrent gas and liquid flow in a system that is representative of the fuel-cell environment. The ideal term modifies the effective diffusivity to account for saturation. The filling of pores can be viewed as causing the traditional effective-diffusion correction term, ε/τ, to be a function of saturation. The more porous the material and less tortuous the pathway, the easier material can be transported through the medium and vice versa. ε/τ ranges from 0 for a solid material to 1 for open space. An effective-diffusion term that directly incorporates saturation is better than using P_C-S relations because the effective diffusion term would remove the middle step of determining P_C. Such a term would elucidate the direct relationship between

flooding and reactant starvation. The remainder of this section discusses how to design an experiment to measure effective diffusion and the considerations necessary for success. What follows are the pioneering steps taken toward this end with hopes that these findings provide a foundation for further development.

The ideal design mimics the fuel-cell environment with two-phase counterflow in which the flows are decoupled. The key differentiation and advantage of this system over a fuel-cell system is the ability to control independently the gas and liquid phases and thereby avoid the reaction-flooding-starvation feedback loop that occurs under normal fuel-cell operation. Liquid would be added to the system from the same face at which reactant gas is monitored. One way to monitor gas transport is via electrochemical reaction. A fast electrochemical reaction should be chosen such that the system is mass-transfer limited. Electrochemical sensing is convenient because the driving force for reactant transport and consumption would be the same as that in a fuel-cell system, and the current provides an indicator of how much gas is reaching the catalytic surface. A second advantage is the proximity of the measurement site to the reaction site. The signal from a limiting current measurement would be easier to interpret than the signal from gas chromatography (GC) for example, because, in the case of using a GC, the gas sampling would be occurring at a location removed from the surface of the DM. Next, to ensure that the system is mass-transfer limited, a proxy gas is desired that reacts quickly and does not produce water. Hydrogen satisfies both of these requirements and is already set-up for use in fuel-cell test stands; thus it is a natural candidate for initial consideration. As a preliminary design, a hydrogen pump set-up is envisioned as shown in Figure 4.1: hydrogen is oxidized at the anode, travels across the polymer-exchange membrane as protons, and recombines as hydrogen on the other side. When catalyzed, the hydrogen reaction is faster than the oxygen reduction reaction, which typically occurs in a fuel cell, and also does not produce water. The system is run at high humidity, >80%, to prevent dry-out of the membrane by osmotic water flux and evaporation.

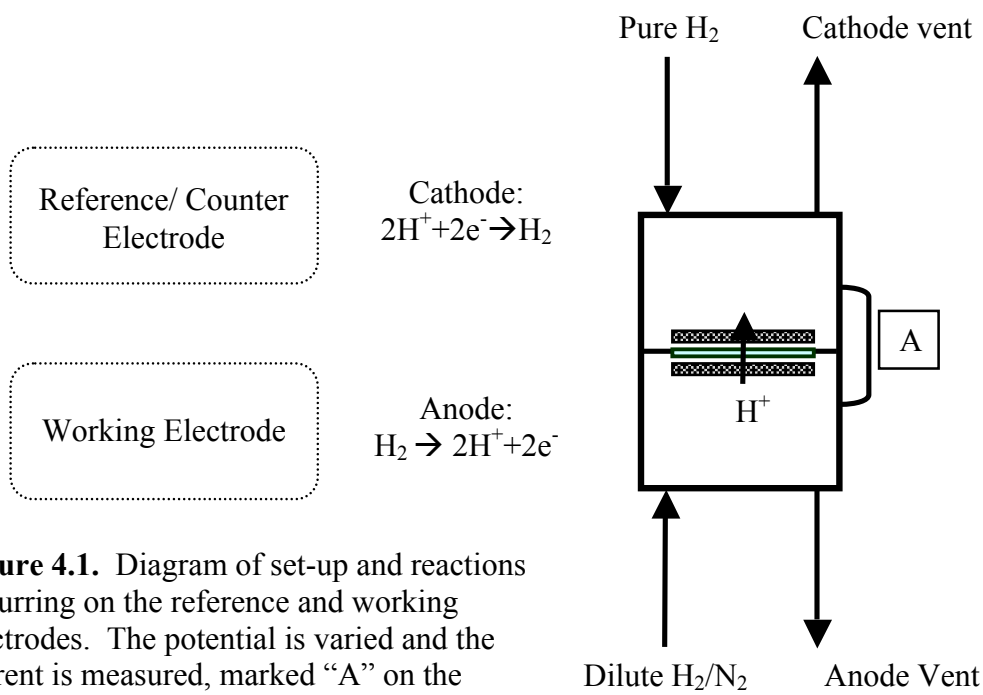

Figure 4.1. Diagram of set-up and reactions occurring on the reference and working electrodes. The potential is varied and the current is measured, marked "A" on the diagram.

4.2 Theory

The next step is to determine how to relate limiting current measurements to effective diffusion. We start with the Stefan-Maxwell equation that describes multicomponent diffusion. 3 species are assumed to be in the system: hydrogen, nitrogen, and water vapor. The first two are fed into the system, and water vapor is present due to the presence of liquid water. The hydrogen flux will be driven by consumption of the hydrogen at the catalytic surface, and there will be counterdiffusion of the inactive species. The inactive species, nitrogen and water vapor, are lumped, resulting in the following Stefan-Maxwell equation:

$$\nabla x_{H_2} = \frac{x_2 \mathbf{N}_{\mathbf{H_2}} - x_{H_2} \mathbf{N}_{\mathbf{2}}}{\mathrm{c_T} \frac{\varepsilon}{\tau}_{\mathrm{eff}} D}$$

where the subscripts H_2 and 2 denote hydrogen and the nitrogen-water species respectively, x is the mole fraction, $\mathbf{N}$ is the flux, c_T is total concentration, ε/τ_{eff} is the saturation-dependent effective diffusivity correction, and D is the single-phase diffusion coefficient adjusted for temperature and gas composition. The saturation dependent term is redefined for this work. The saturation can be imagined to affect both the porosity and tortuosity such that ε/τ is a function of saturation. Therefore, rather than include a constitutive relation as a saturation-correction factor, ε/τ_{eff} is defined to include saturation effects.

The second term is assumed to be negligible compared to the first because low initial hydrogen concentrations will be used, namely, below 4% in general and below ≤0.1% in particular. The desire for low hydrogen concentrations stems from two fronts: hydrogen combustibility is not of significant concern <4% and, because of the fast diffusion of hydrogen, a low initial concentration is used to ensure a mass-transfer limitation. Concentrations ≤0.1% were found to be sufficient. With this assumption and substitution of the ideal-gas law for the concentration, the equation can be rewritten as

$$\nabla x_{H_2} = \frac{x_2 \mathbf{N}_{\mathbf{H_2}} - x_{H_2} \mathbf{N}_{\mathbf{2}}}{\mathrm{c_T} \frac{\varepsilon}{\tau}_{\mathrm{eff}} D} \cong \frac{x_2 \mathbf{N}_{\mathbf{H_2}}}{\mathrm{c_T} \frac{\varepsilon}{\tau}_{\mathrm{eff}} D} = \frac{x_2 \mathbf{N}_{\mathbf{H_2}}}{\frac{\mathrm{P}}{\mathrm{RT}} \frac{\varepsilon}{\tau}_{\mathrm{eff}} D}$$

where P is total pressure, R is the universal gas constant, and T is the temperature.

The hydrogen flux is found from the limiting current and Faraday's law, and an averaged x_2 value from assuming a linear gradient is substituted to obtain the final equation,

$$\frac{x_{H_2}^0 - 0}{\delta} = \frac{(1 - 0.5 x_{H_2}^0) \frac{i_{\mathrm{lim}}}{2\mathrm{F}}}{\frac{\mathrm{P}}{\mathrm{RT}} \frac{\varepsilon}{\tau}_{\mathrm{eff}} D}$$

where the 0 subscript denotes initial value, δ is the diffusion length, and i_{lim} is the limiting current. The above can be rearranged such that a plot of the left side versus limiting current has a slope that is the inverse of the effective diffusion coefficient:

$$\frac{x_{H_2}^0}{(1-0.5x_{H_2}^0)}\frac{2PF}{\delta RT}D = \left(\frac{\varepsilon}{\tau_{\text{eff}}}\right)^{-1} i_{\text{lim}} .$$

All parameters on the left side are known, and the limiting current is measured for several different initial hydrogen concentration values. $\varepsilon/\tau_{\text{eff}}$ can be found by fitting a line to the data and calculating the inverse of the slope.

4.3 Design Considerations

There are two common design errors to bear in mind when embarking upon the design process. First, the ideal design would be one in which there is an open chamber below the DM to remove gas-channel effects and water condensation in the channels. However, in order to achieve adequate electrical contact between the different layers, the DM and membrane-electrode assembly (MEA) must be compressed together in spacings no larger than roughly 2 mm, thus requiring use of the standard flow-channel design used in fuel cells. Use of hard materials, even 2 cm plates of solid stainless steel, was found to be insufficient to ensure compressive contact over a 5 cm diameter circular area. Second, a reference electrode is necessary for successful implementation of an electrochemical sensing approach. This seems a trivially obvious statement and yet is easily neglected. When running the hydrogen-pump set-up, the initial thought is to run a dilute hydrogen-nitrogen mixture over the working electrode at which the hydrogen will dissociate. A nitrogen flush is envisioned for the counterelectrode where protons will recombine to form hydrogen. This layout minimizes hydrogen cross-over and uses the hydrogen reaction, which is commonly used as an electrochemical standard. As such, the design may sound reasonable. However, this simple layout has a deceptively simple flaw; there must be a sufficient level of hydrogen at the counterelectrode in order for the electrode to function as a reference. Pure nitrogen and the small amount of hydrogen produced at the counterelectrode lead to a floating potential that will not give an accurate baseline for voltage and complicates the search for limiting current.

Because hydrogen is necessary on the counterelectrode side, the polymer-exchange membrane (PEM) must provide a physical barrier to prevent gas crossover. The barrier prevents hydrogen for the reference electrode from crossing to the working-electrode side and artificially increasing the limiting current. This also means that the PEM cannot be perforated to enable controlled counterflow of liquid water. Without the use of a more elaborate design, water cannot be introduced from the reference-electrode side because the PEM is not sufficiently permeable to water, and water cannot be introduced from the working-electrode side due to the hydrogen feed. The most challenging portion of the design is determining how to introduce liquid water into the system in a controlled fashion so that the saturation is known. A recommendation regarding how to develop custom a component to introduce water will be discussed. Once water is introduced in a controlled fashion, one can adjust for the effects of electroosmotic drag by using the limiting current measurement to determine the number of protons that have moved across the PEM.

The presence of hydrogen on the reference-electrode side also means that hydrogen crossover will occur from the reference-electrode to the working-electrode side and increase the current. A cyclic voltammagram (CV) of a hydrogen-nitrogen system is measured to determine the contribution from crossover. For a CV, the working electrode potential is swept linearly and reversed over a specified range, and the current is measured. A CV can be used to diagnose a system and show where certain reactions are occurring. A typical hydrogen adsorption-desorption CV can be found from the literature and is shown in Figure 4.2.[88] The upper curve moving from low to high potential shows the hydrogen desorption from the platinum surface into protons while the lower curve shows the current produced as hydrogen is adsorbed onto the catalytic surface and eventually turned into hydrogen gas. The separation between the forward and reverse lines in the 0.4 to 0.6 V region is due to double-layer charging effects. In a perfect system, the 0.4 to 0.6 V range is centered around zero current. The offset between the zero-current-density line and the flat regions of the curve is due to hydrogen crossover. The CV scans should look similar to the one shown in Figure 4.2 in the presence of a stable reference potential. This baseline curve will be subtracted from proton-pump CVs to find limiting current. By doing so, the current due to cross-over is subtracted, and the true limiting current due to hydrogen mass-transfer limitations remains. The process must be repeated for each MEA because different MEAs will vary in their degree of crossover. All experimental parameters, temperature, humidity, flow rates, pressure, and CV scan rate, should be the same between baseline and limiting-current measurement.

The final check before starting experiments is to confirm that when the cell is run in proton-pump mode at the lowest planned hydrogen concentration, the resulting limiting current is below the starvation limit, corresponding to complete consumption of all hydrogen that is introduced into the system. The current should be limited due to transport, not due to lack of reactant. Conversely, the hydrogen concentration should also be low enough that a mass-transfer limitation exists; if the concentration is too high, the high diffusion of hydrogen may prevent the onset of a limiting current.

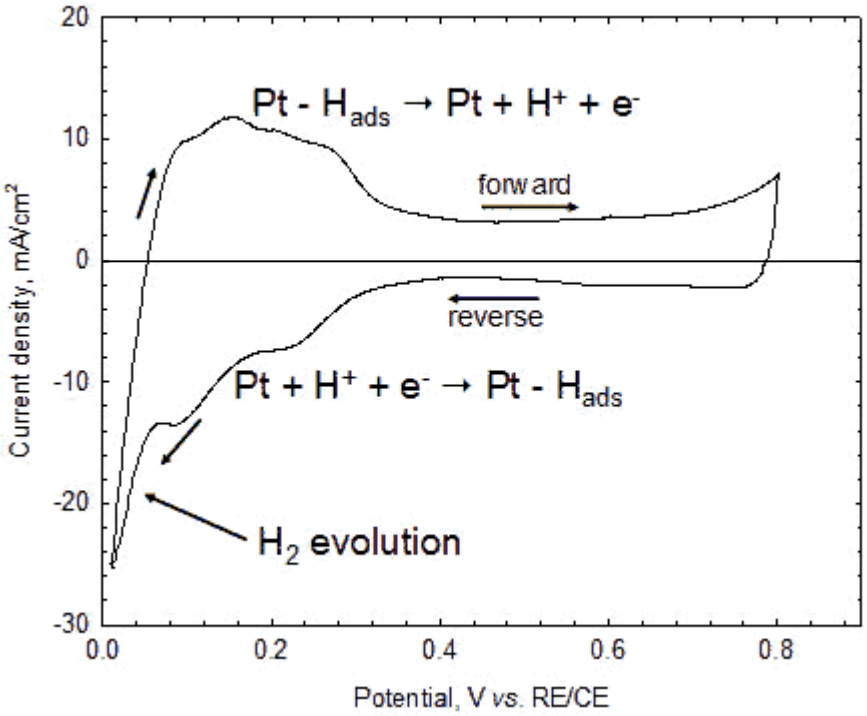

Figure 4.2. CV of PEM fuel-cell catalyst layer that shows hydrogen adsorption and desorption. Conditions: Scan rate = 40 mV/s; Cell: 35°C; 100% relative humidity anode/cathode; 1 atm.[88]

4.4 Results and Analysis

The tests were run in a custom-made cell that had a 2.25 cm^2 active area and parallel flow channels. The cell was assembled with a Gore Primea MEA with 0.1 and 0.2 mg Pt / cm^2 on the reference and working electrode, respectively. CVs were taken at 20 and 50 mV/s for comparative purposes. Both scanning speeds yielded reasonably similar results; a scan rate of 50 mV/s led to slightly cleaner results, in that the final limiting current versus voltage curve collapsed onto one curve, and was therefore the preferred scan rate. For initial testing purposes, 3 DMs with 2 thicknesses and 2 polytetrafluoroethylene (PTFE) weight loadings were assembled for the fuel cell. These DM were tested at 80 C in different experimental conditions that varied water content in the cell. Controlling the water content is challenging because water cannot be introduced manually into the working-electrode side through a perforated PEM. For these initial experiments, an alternative was to introduce the gas feed at 150% relative humidity (RH) in the event that water would condense on the GDL fibers. Another approach was to run the system in fuel-cell mode first and produce water on what would later become the hydrogen-splitting side. Water was generated at levels corresponding to 0.6, 1, and 1.5 A/cm^2 for 20 minutes. The oxygen side was purged with nitrogen, and then the proton pump experiment was started. For each condition, the hydrogen concentration was varied to generate several points for the graph and find ε/τ_{eff}. These approaches are not a substitute for a system that allows controlled saturation, but are used to test the limiting-current approach under various conditions to observe how DM with different manufacturing specifications respond. The matrix of inputs is shown in Figure 4.3, and a sample of data used to find ε/τ_{eff} is shown in Figure 4.4.

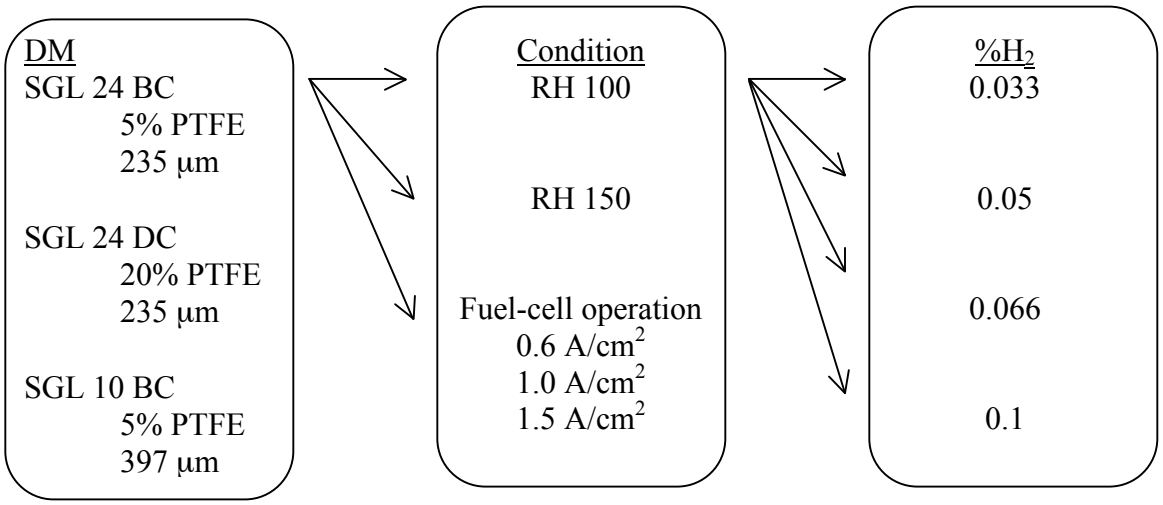

Figure 4.3. Matrix of the experiments run using various DM, operating conditions, and hydrogen concentrations on the working electrode. All DM have a 23% PTFE MPL. The cell was operated at 80 C.

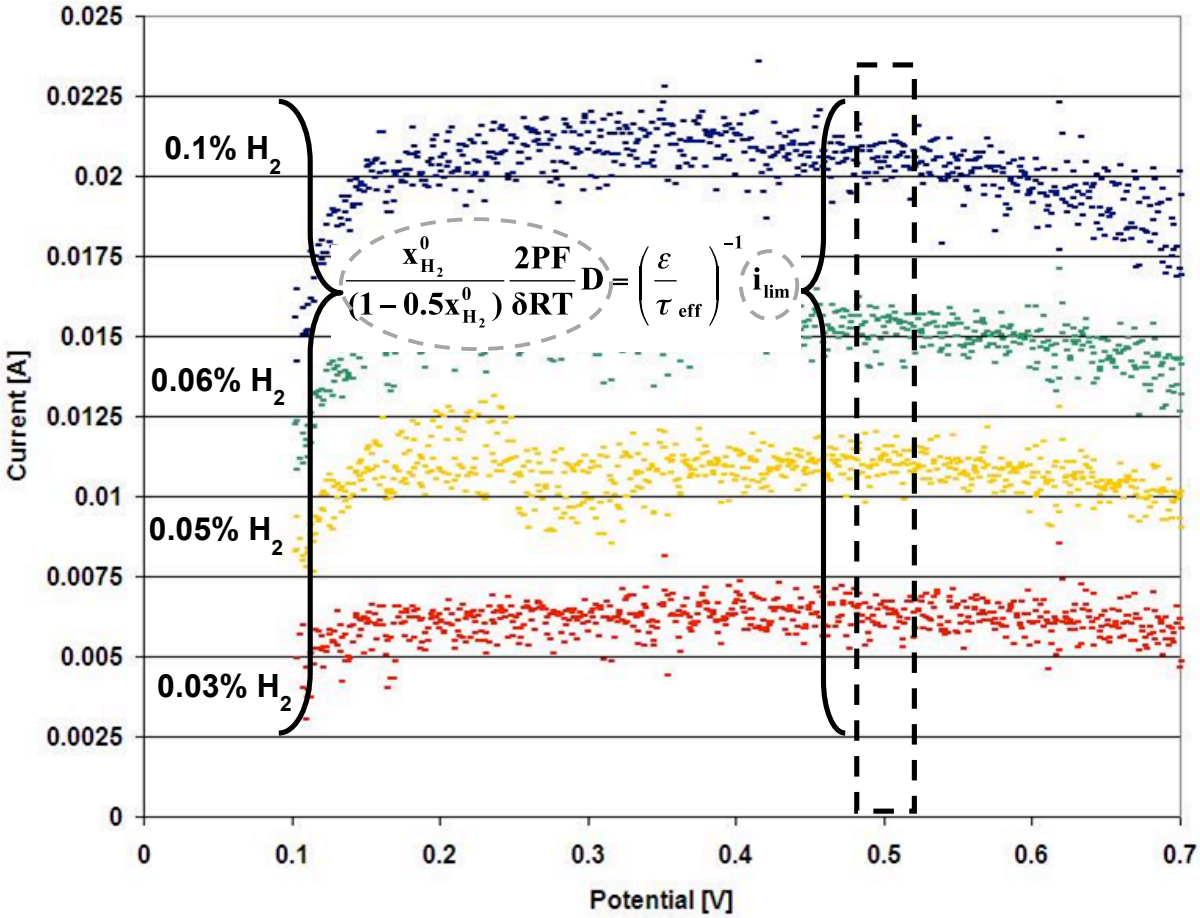

Figure 4.4. Data collected for SGL 24 BC operated at 80 C and 100% RH after subtracting the baseline CV that accounts for current due to crossover. The hydrogen concentration fed to the working-electrode side is known and enables calculation of the left side of the equation. Limiting current is taken as the average current between 0.48 to 0.52 V and substituted into the right side. Regression of data points taken at different hydrogen concentrations provides the slope, e.g., the inverse of the effective diffusion.

Preliminary results indicate that this approach is valid: the observed limiting current was less than that of the starvation limit, and ε/τ_{eff} was successfully found for each scenario and shown to decrease in the presence of water. ε/τ_{eff} values for different DM operated under several conditions are shown in Table 4.1 with a subset of those results plotted in Figure 4.5. Comparison of results from running the cell at 200 and 300 ml/min shows that higher flow rates at the same gas composition increase current output for all DM tested. Higher flow rates increase convective flux which leads to higher limiting currents than would be achieved with diffusion-limited transport. To decrease convection, the lower flowrate, 200 ml/min is used for all other measurements. A comparison of each DM's output at 200 ml/min under different conditions—100% RH, 150% RH, and after 20 min of water production at 0.6 A/cm^2—demonstrates that the thicker the DM, the greater the variability in ε/τ values in different conditions; although the thickest DM has the highest ε/τ_{eff} at high gas flowrate, it also has the lowest in high-RH conditions. The difference between 5 and 20% PTFE samples of the same

thickness was not as great. The advantage of adding PTFE may be obvious when shifting from none to some, but 20% PTFE may be too high to capture significant additional benefit from making the GDL more hydrophobic and instead compromise electrical contact. Nonetheless, all DM exhibit different ε/τ_{eff} values depending on the operating conditions. Therefore, the choice of the best DM involves a trade-off between optimization for a particular condition and general robustness.

Table 4.1. ε/τ_{eff} and intercept values were calculated for 3 cells made with SGL DM. Total flow refers to the gas-flow rate on the side of the working electrode. Scan rate of the CV is given for readings taken at 20 or 50 mV/s. FC mode refers to the A/cm^2 pulled on the cell for 20 minutes prior to flushing of the system and switching to proton-pump mode.

Cell	Total Flow (ml/min)	RH (%)	scan (mV/s)	FC mode (A/cm^2)	ε/τ_{eff}	intercept
SGL 24 BC	200	100	20		0.04737	0.011401
5% PTFE	200	100	50		0.046686	-0.00634
235 μm	300	100	20		0.059017	-0.00703
	200	100	20	0.6	0.066194	0.053493
	200	148	50		0.080165	0.120891
	200	100	50		0.046686	0.001176
SGL 24 DC	200	100	50		0.048757	0.019328
20% PTFE	300	100	50		0.05858	0.005355
235 μm	200	100	50	0.6	0.038769	0.071181
	200	100	50	1	0.039691	0.037088
	200	100	50	1.5	0.03301	0.030604
	200	113	50		0.050817	0.023611
	200	113	50	1	0.066747	0.087614
	200	148	50		0.043867	0.01328
	200	148	50	1	0.034212	0.033157
SGL 10 BC	200	100	50		0.057037	0.008423
5% PTFE	300	100	50		0.083504	-0.13773
397 μm	200	100	50	0.6	0.078537	0.072363
	200	100	50	1	0.080046	0.07974
	200	100	50	1.5	0.055364	0.04821
	200	113	50		0.065056	-0.17593
	200	148	50		0.034269	-0.28358
	200	113	50	1	0.055368	-0.19159
	200	148	50	1	0.047103	-0.17747

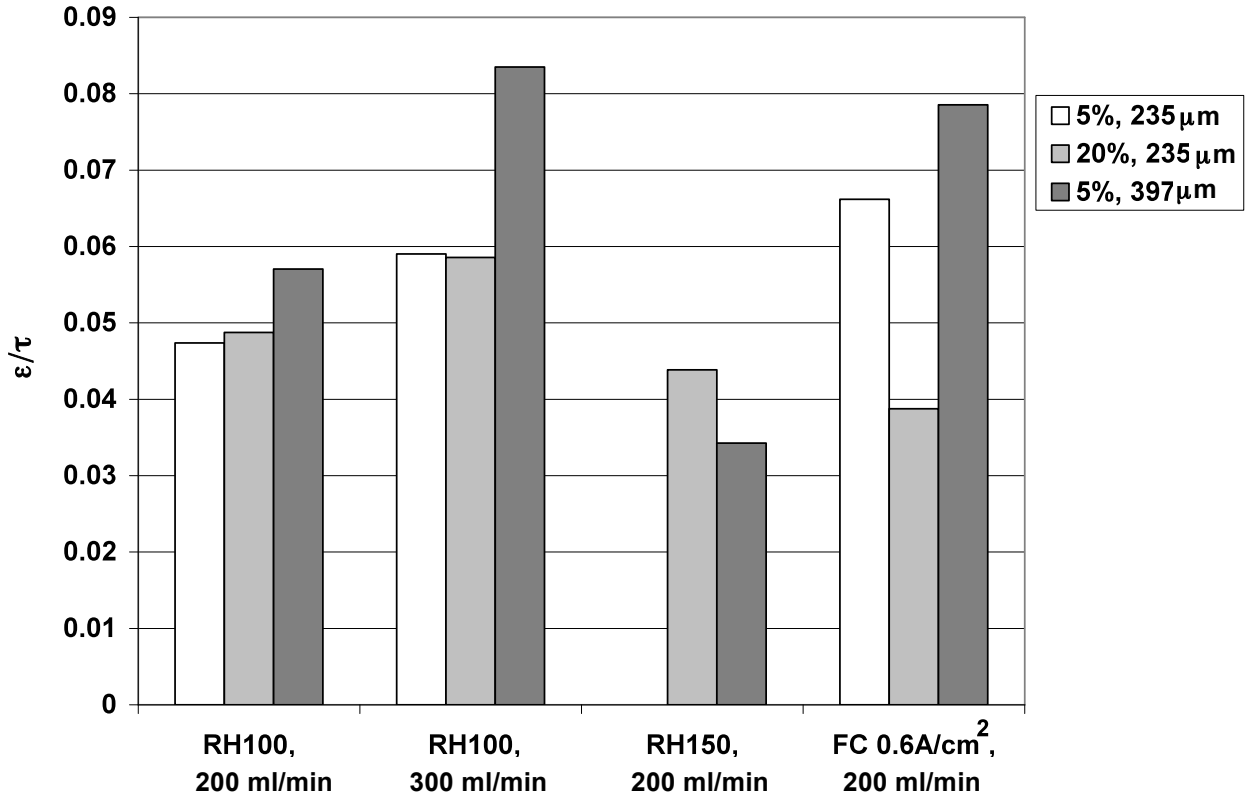

Figure 4.5. Effective diffusion coefficients are shown for SGL DM tested in conditions with different RH, flowrate, and post fuel-cell (FC) operation. SGL DM characteristics, PTFE loading and DM thickness, are indicated in the legend. DM respond differently based on the operating conditions.

The low ε/τ_{eff} values can be analyzed by recognizing that the GDL and MPL will have different contributions to the overall ε/τ_{eff}. The MPL is thinner, but has lower porosity and smaller pores than the GDL, and is hence likely to contribute more resistance to transport. To develop an intuition for the contribution from the GDL and MPL, the total resistance is assumed to be a sum of the individual resistances being added in series,

$$\frac{\delta_{Total}}{\varepsilon/\tau_{eff}} = \frac{\delta_{GDL}}{\varepsilon/\tau_{GDL}} + \frac{\delta_{MPL}}{\varepsilon/\tau_{MPL}}.$$

The total resistance is taken from the measurements, and the GDL resistance is taken from the literature because limiting-current measurements with only a GDL had not been run. In the literature, impedance spectroscopy is used to back out the single-phase ε/τ_{abs} term which is not a function of saturation.[38, 89] The sample is filled with electrolyte, and the voltage is varied at different frequencies. A combination of high- and low-frequency signals is applied to distinguish between charge transfer through the electrolyte and through the conductive carbon fibers of the DM, and also account for double-layer charging effects next to the conductive fibers. The experiment cannot be applied to a water-saturated system because an electrolyte is necessary; values borrowed from impedance spectroscopy measurements are therefore going to

be higher than values determined via the limiting-current approach, which includes saturation. The calculated MPL resistance will therefore serve as an upper bound of the MPL contribution. For the base-case scenario of SGL 24BC, ε/τ_{eff} is 0.047, and ε/τ_{GDL}, taken from Fluckiger's work,[38] is 0.3. The thicknesses of the GDL and MPL in a compressed SGL 24BC sample are approximated as 150 and 50 μm, respectively. This results in an ε/τ_{MPL} value of approximately 0.01. This means that roughly 85% of the resistance to flow in a DM comes from the MPL. This is in line with the intuitive logic that in the absence of liquid, the MPL offers the highest resistance to flow due to the lower porosity and smaller pore sizes. This would change as liquid builds up in the system because water is more likely to build-up in the more porous, more hydrophilic GDL, and is also expected to be transported in vapor form across the MPL and deposit in the GDL. As saturation increases, ε/τ_{eff} will become increasingly dependent on the resistance of the GDL. Future tests should therefore study GDLs in isolation to better pinpoint the changes in transport properties as a function of saturation.

4.5 Recommendations and Outlook

The procedure for optimizing experimental design is explained. First, confirm that the apparatus chosen for these measurements provides sufficient contact for proper operation of the MEA. A common temptation is to design a chamber-like open area over the face of the DM on the working electrode; the intention is to remove channel effects. However, a chamber design is less likely to ensure an even pressure distribution over the face of the MEA. If a nontraditional cell is made, impedance spectroscopy and pressure paper can be used to check the contact resistance and pressure distribution.

Second, once the hardware is tested, determine the minimum level of hydrogen necessary on the reference electrode side to maintain a reliable reference-electrode reading. The driving force for crossover, a concentration gradient, is minimized by using the smallest concentration of hydrogen necessary on the reference-electrode side. In the case of pure hydrogen, the cross-over through an 18 μm Gore membrane constitutes 60 to 80% of the limiting current signal from an experimental run. This base-level signal can be subtracted with good reproducibility, but should be reduced to minimize the influence of the baseline on final results. CVs are run on a hydrogen-nitrogen system, and the hydrogen concentration is incrementally lowered until the minimum concentration required for a stable reference is found.

Lastly, one should check the limiting current using different flow rates of hydrogen at constant concentration. The objective is to minimize the flow rate to reduce convective flux while also providing enough hydrogen to prevent starvation and uneven hydrogen levels down the length of gas-flow channels. If the hydrogen feed rate is too low, the cell will reach a starvation limit. If it is too high, convective effects will skew the diffusion measurements. The flow rate can by determined by recording the limiting current of a particular hydrogen concentration and taking measurements at different flow rates. The optimal flow rate is the lowest flow rate at which the observed limiting current does not change appreciably with increasing flow rate and is above the starvation and measurement limit.

Tests should treat GDLs in isolation, i.e., without MPLs, run at a maximum of 100% RH. Using RHs above 100% or running the system in fuel-cell mode beforehand are not productive means of changing the water content in the GDL. Such water-loading attempts resulted in the formation of water slugs in the channels and tubing and were shown to produce erratic values. Water cannot be guaranteed to be in the GDL exclusively. One approach to externally introducing water into the system could be the use of a stiff, patterned hydrophilic and hydrophobic material. The traditional solid metal ribs would be replaced with hydrophilic material that would allow water to be introduced while preventing gas from exiting by the same pathway. The hydrophobic material would allow hydrogen gas to reach the MEA by preventing flooding of the gas pathway. The design would be similar to a carbon water-transport plate (WTP) with gas channels that are filled with a hydrophobic material. A modified WTP is well-suited for this experiment because it meets the structural, electrical, and functional criteria—it is a rigid plate that can apply compression, it is conductive and thus functions as a current collector, and it has small hydrophilic pores that enable selective water transport.

In conclusion, the advantage of calculating transport properties through an electrochemical sensing technique is that the signal is easy to convert to a flux and the system can be tested in-situ with saturation. Preliminary work successfully demonstrates a proof of concept and that ε/τ_{eff} can be determined for different systems under various conditions. The results are easier to interpret than those obtained through impedance spectroscopy because the electrical conductivity of the carbon fibers does not influence output signal, as is the case in impedance spectroscopy. However, the limiting-current technique is yet in a formative stage and requires more fine-tuning before yielding quantitatively significant results. The set-up used for these experiments was sufficient to show a proof of concept, but could not be used for controlled-saturation experiments. Design revisions with patterned materials, such as a modified WTP, should be developed to improve control of saturation levels in DM. Qualitatively, initial tests suggest that DM choice should consider the balance between specific optimization versus general robustness, and that MPLs contribute significantly to transport resistance. Refinement of the technique should enable a dynamic measurement of effective diffusion as a function of saturation and provide a realistic and informative understanding of two-phase transport.

Chapter 5.

5.1 Conclusions

5.1.1 Diffusion Media

Understanding two-phase transport in fuel cells requires an understanding of fuel-cell diffusion media (DM), complex materials with significant physical and chemical inhomogeneities. DM provide a unique challenge to traditional porous-media studies due to their high porosity, fibrous and nonideal structure, and uneven wettability distribution. Toward the end goal of developing experimentally validated, diffusion-media-specific relationships and recommendations, the objective of this work has been to elucidate first, how DM differ in water uptake and ejection properties, second, what factors cause differences and their relative importance, and third, how DM transport properties can be ascertained in a representative, in-situ environment.

Capillary-pressure versus saturation (P_C-S) measurements were used to quantify water uptake and retention experimentally in a controlled setting. A comparison between gas-injection and liquid-injection methods demonstrated fairly good agreement in results, and also highlighted different strengths and points of consideration. The gas-injection method provides steady-state measurements and is easier to execute, e.g., fluctuations due to disturbances do not have repercussions on the final steady-state measurement. The liquid-injection method is the preferred method if one wishes to probe higher P_C, and the key point is to account for the presence of an air bubble through application of a simple ideal-gas-law correction. The P_C-S curves of DM show that DM are neutrally wetting and require excess pressure for both injection and withdrawal of water. The implication of this wetting hysteresis on fuel-cell operation is that preventing water from accumulating is easier than attempting to withdraw it once the DM is saturated. Although each manufacturer produces DM that are neutrally wetting, DM from SGL, Toray, Freudenberg, and MRC each have a signature feature in their P_C-S curves, such as low

residual-saturation levels or a high degree of hysteresis between injection and withdrawal responses.

Visual-imaging results elucidated sources for these differences and provided clues for directing development of finer-tuned DM. The first factor for variation is the underlying structure of the DM fibers and binder. Scanning-electron-microscopy (SEM) images showed noticeable structural discrepancies in fiber density and orientation, which in turn influence polytetrafluoroethylene (PTFE) deposition. SGL has large surface pores and a rough binder surface. Toray and MRC have similar fibrous structures, but Toray's binder and PTFE deposits in sheets whereas MRC's deposition process creates a secondary pore structure. The secondary pore structure is expected theoretically to widen the P_C-S curve because the addition of a secondary structure in general means that a wider distribution of pores will fill at different times, and the introduction of smaller, hydrophobic pores in particular makes the sample more hydrophobic. This hypothesis is confirmed experimentally by the higher P_C required for water to enter MRC samples during P_C-S tests. Freudenberg's manufacturing process is of most interest because its looped, cleanly annealed fibers may be key to achieving full water removal. An interesting pursuit from a manufacturing perspective could be to combine the low residual saturation achieved by Freudenberg and the high hydrophobicity created by MRC to develop a DM that is both harder to flood and easier to drain. The observed underlying structure of untreated DM was thus found to corroborate inferences from P_C-S measurements and yielded both manufacturing insight and theoretical validation.

PTFE loading is another factor that would be expected to influence water-uptake behavior because the intention behind adding more PTFE is to make the medium more hydrophobic. However, a consideration of P_C-S and mercury-intrusion-porosimetry (MIP) results indicates that the initial addition of PTFE can shift the DM from hydrophilic to hydrophobic according to the US Bureau of Mines wettability index, but subsequent addition of PTFE serves to reduce porosity without significantly increasing hydrophobicity. Porosity decreases precipitously when the loading is above 60%, probably due to the formation of PTFE-enclosed spaces that create dead volume. High PTFE loading is counterproductive because electrical conductivity is compromised and porosity is reduced, leading to poorer transport within the material.

Lastly, variation between samples of the same type is manifest to different degrees depending on the manufacturer. Results for DM from different manufacturers must be considered in the context of product variation between DM from the same manufacturer. In particular, a systematic MIP study revealed that pore-size distributions (PSDs) of SGL samples showed more variation between samples of the same type than did Toray samples that had 0 to 50% PTFE deposition. Because unintended variation may be of similar or greater magnitude than intentional variation, tests involving SGL samples in particular should be repeated or conducted on large samples, >4 cm^2, to achieve statistically conclusive results. Complete parametric studies are difficult to conduct due to time and cost considerations, but a collection of measurements from this study has shown that PTFE can impart morphological changes to the DM either in the form of decreased porosity, as shown by the Toray measurements, or preferentially filling smaller pores, as suggested by the SGL measurements.

In addition to these macroscale variations between DM, microscale nonuniformities within the DM are important when considering whether and where water may accumulate preferentially in the DM. Energy-dispersive X-ray (EDX), microtomed SEM, and synchrotron-radiation images show through-plane variation in the DM. The density and PTFE distribution is highest on the outer edges and lowest in the center. For simulations to capture simply yet realistically the structure and wettability of DM, a preliminary approximation should divide the gas-diffusion layer (GDL) portion of the DM into 3 regions, two denser, more hydrophobic layers on either side of a third layer. Although the current state of synchrotron-radiation images is best suited for qualitative analysis, advancements in beam, equipment, and post-processing techniques are promising. Present-day images are sufficient for showing how the GDL switches from hydrophobic to hydrophilic during injection and withdrawal respectively. Improvements in structure reconstruction and phase contrast are of particular interest to enable more computerized phase-parsing and quantitative analysis.

5.1.2 Catalyst Layers

The wettability and water-uptake behavior of catalyst layers (CLs) in isolation was examined for the first time. CLs are difficult to study due to their low pore volume when made of normal thickness, and crack formation when made 2 to 3 times thicker. In-house CLs were made according to the CL-ink protocol of Los Alamos National Laboratory and painted directly onto porous hydrophobic membranes to enable isolated P_C-S measurements of CLs. These CLs were found to be highly hydrophilic, reaching 80% saturation at zero P_C. The addition of Pt had a greater effect on the CL than did protonation of the Nafion therein, and increased hydrophilicity of the sample. Decreasing the Pt loading can therefore be useful both for meeting Pt loading targets and also reducing water attraction.

Preliminary studies with commercial CLs from Ion Power demonstrated two effects of creating thicker CLs on P_C-S curves. First, increasing the thickness of the CL introduces greater pore-type and size variation as evinced by the wider P_C-S curve that denotes uptake occurring over pores that are filling at different pressures. This means that additional layers of CL ink are changing the overall CL features. Second, the cracks that form on especially thick samples are preferentially wetting and shift dramatically the P_C-S curve into the hydrophilic. Contrary to the smooth samples that showed most water movement in the positive P_C range and reached residual saturation levels by -20 kPa, the thicker, cracked sample retained roughly 50% of its cyclable water volume at the same pressure. Morphology plays a key role and causes the greatest shift in hydrophilicity. Future saturation studies should focus on morphological changes due to crack formation and the effect of cell assembly and aging on the CL structure.

5.2 Perspective and Future Work

Ensuring proper water management in fuel cells is challenging because the solution lies at the intersection of several complex studies: heterogeneous porous media, fibrous media, two-phase flow, and fuel-cell operation. Prioritization is important in this situation to define a tangible problem; significant contributions can be made through an investigation that focuses on two or three of the four mentioned areas, and is better poised for success. The problem with the

use of DM for fundamental studies of heterogenous fibrous media is two-fold: first, the DM is highly nonideal and second, one cannot gain access to DM production capabilities to make ideal structures. One is therefore at the mercy of the manufacturer both in terms of type of sample provided and details divulged, if any, regarding the production process.

If the goal is to understand wettability of DM on a fundamental level, then the research project should start from fundamental roots. Significant work on fibrous modeling has been done by Thompson,[48] Tomadakis,[90-92] and others.[51, 93-96] The field would benefit from experimental data from fibrous materials of more uniform structure and wettability. Structural effects could be studied in isolation, and the effect of fiber density and orientation could be observed in P_C-S curves and MIP results. Simulations could incorporate density and orientation effects by using P_C-S and PSD outputs or, depending on the progress of synchrotron imaging of fibrous materials, import a fibrous structure and attempt to match the measurements. Once agreement is achieved, one can feel more confident that the assumptions inherent in many of these models, namely that the pores can be simplified to equivalent cylindrical pores, are grounded in a realistic foundation. An exciting experimental and theoretical project would be to build on the work by Payatakes[97] and Prat[98] by creating an ideal fibrous micromodel with a mixture of wetting and nonwetting fibers. Fluid invasion could be imaged, and the P_C response could be tied back to the overall structure and orientation of fibers and their wettability. The objective is to take a holistic approach incorporating heterogeneities, fibrous media, and two-phase effects to create, characterize, and simulate a material. The PSD and P_C-S outputs and fits can be analyzed and attributed directly to controllable properties, eventually creating the predictive capability needed to prototype well-defined materials via simulation rather than experiment.

If the objective is to characterize two-phase flow in fuel-cell systems in particular, then the focus shifts from casting idealized systems into mathematical constructs to starting with commercially available DM and developing empirical relationships. Preliminary proof-of-concept work has demonstrated that effective diffusion can be determined electrochemically via a limiting-current proton-pump experiment. Given a series of limiting current data for different hydrogen inlet concentrations, ε/τ_{eff} can be calculated for DM under various operating conditions. The relative resistance to transport varies between the DM, depending on the specific conditions. Therefore, the choice of the optimal DM will involve a trade-off between optimization for a particular condition versus general robustness. Initial results indicate that the microporous layer (MPL) may contribute up to 85% of the transport resistance in the absence of liquid water. However, further studies of GDLs in isolation should be conducted because as liquid water accumulates in the GDL, the GDL is expected to be a source of transport resistance. Several operational and design recommendations have been made to enable and facilitate future research. Specifically, the hydrogen concentration on the reference-electrode side of the proton-pump experiment and the flow rate of the hydrogen feed on the working-electrode side should be minimized to reduce cross-over and convection, respectively. A means of knowing and controlling water content is necessary to determine ε/τ_{eff} as a function of saturation. Design revisions with selectively hydrophilic and hydrophobic materials will enable controlled introduction of liquid water. By collecting ε/τ_{eff} values for different GDLs under different conditions, one will be able to determine empirically effective transport properties as a function

of saturation. These data can be incorporated directly into full fuel-cell simulations to predict performance and determine quickly the optimal DM for a given environment.

References

1. Ballard, Specification sheet for FCgen1020ACS, www.ballard.com/fuel-cell-products, Accessed October, 2011.
2. A. Z. Weber, R. Balliet, H. P. Gunterman and J. Newman, in *Modern Aspects of Electrochemistry*, ed. M. Schlesinger, Springer, New York, 2009, vol. 43, p. 273.
3. A. Z. Weber, R. M. Darling and J. Newman, *Journal of the Electrochemical Society*, 2004, **151**, A1715-A1727.
4. C. Y. Wang, *Chemical Reviews*, 2004, **104**, 4727-4765.
5. N. Djilali, *Energy*, 2007, **32**, 269-280.
6. A. Z. Weber and J. Newman, *Journal of the Electrochemical Society*, 2005, **152**, A677-A688.
7. X. L. Wang, H. M. Zhang, J. L. Zhang, H. F. Xu, Z. Q. Tian, J. Chen, H. X. Zhong, Y. M. Liang and B. L. Yi, *Electrochimica Acta*, 2006, **51**, 4909-4915.
8. J. T. Gostick, M. A. Ioannidis, M. W. Fowler and M. D. Pritzker, *Electrochemistry Communications*, 2009, **11**, 576-579.
9. M. S. Wilson, J. A. Valerio and S. Gottesfeld, *Electrochimica Acta*, 1995, **40**, 355-363.
10. N. Hara, K. Tsurumi and M. Watanabe, *Journal of Electroanalytical Chemistry*, 1996, **413**, 81-88.
11. G. J. M. Janssen and M. L. J. Overvelde, *Journal of Power Sources*, 2001, **101**, 117-125.
12. K. Karan, H. Atiyeh, A. Phoenix, E. Halliop, J. Pharoah and B. Peppley, *Electrochemical and Solid State Letters*, 2007, **10**, B34-B38.
13. Z. G. Qi and A. Kaufman, *Journal of Power Sources*, 2002, **109**, 38-46.
14. E. Passalacqua, G. Squadrito, F. Lufrano, A. Patti and L. Giorgi, *Journal of Applied Electrochemistry*, 2001, **31**, 449-454.
15. V. A. Paganin, E. A. Ticianelli and E. R. Gonzalez, *Journal of Applied Electrochemistry*, 1996, **26**, 297-304.
16. C. S. Kong, D. Y. Kim, H. K. Lee, Y. G. Shul and T. H. Lee, *Journal of Power Sources*, 2002, **108**, 185-191.
17. F. A. L. Dullien, *Porous Media: Fluid Transport and Pore Structure*, Academic Press, New York, 1992.
18. R. B. Bird, W. E. Stewart and E. N. Lightfoot, *Transport Phenomena*, John Wiley & Sons, New York, 2002.
19. J. Newman and K. Thomas-Alyea, *Electrochemical Systems*, John Wiley & Sons, New Jersey, 2004.
20. V. Gurau, M. J. Bluemle, E. S. De Castro, Y. M. Tsou, T. A. Zawodzinski and J. A. Mann, *Journal of Power Sources*, 2007, **165**, 793-802.
21. J. T. Gostick, M. W. Fowler, M. D. Pritzker, M. A. Ioannidis and L. M. Behra, *Journal of Power Sources*, 2006, **162**, 228-238.
22. J. P. Feser, A. K. Prasad and S. G. Advani, *Journal of Power Sources*, 2006, **162**, 1226-1231.
23. E. C. Kumbur, K. V. Sharp and M. M. Mench, *Journal of Power Sources*, 2007, **168**, 356-368.
24. W. S. He, J. S. Yi and T. Van Nguyen, *Aiche Journal*, 2000, **46**, 2053-2064.
25. A. Z. Weber and J. Newman, *Journal of the Electrochemical Society*, 2004, **151**, A311-A325.

26. A. A. Shah, G. S. Kim, W. Gervais, A. Young, K. Promislow, J. Li and S. Ye, *Journal of Power Sources*, 2006, **160**, 1251-1268.
27. U. Pasaogullari, C. Y. Wang and K. S. Chen, *Journal of the Electrochemical Society*, 2005, **152**, A1574-A1582.
28. G. W. Jackson and D. F. James, *Canadian Journal of Chemical Engineering*, 1986, **64**, 364-374.
29. M. V. Williams, E. Begg, L. Bonville, H. R. Kunz and J. M. Fenton, *Journal of the Electrochemical Society*, 2004, **151**, A1173-A1180.
30. B. Markicevic and N. Djilali, *Physics of Fluids*, 2006, **18**, 13.
31. J. Becker, R. Fluckiger, M. Reum, F. N. Buchi, F. Marone and M. Stampanoni, *Journal of the Electrochemical Society*, 2009, **156**, B1175-B1181.
32. D. M. O'Carroll, L. M. Abriola, C. A. Polityka, S. A. Bradford and A. H. Demond, *Journal of Contaminant Hydrology*, 2005, **77**, 247-270.
33. J. H. Nam and M. Kaviany, *International Journal of Heat and Mass Transfer*, 2003, **46**, 4595-4611.
34. M. J. Martinez, S. Shimpalee and J. W. Van Zee, *Journal of the Electrochemical Society*, 2009, **156**, B80-B85.
35. J. I. Gostick, M. A. Ioannidis, M. W. Fowler and M. D. Pritzker, *Journal of Power Sources*, 2007, **173**, 277-290.
36. B. Markicevic, A. Bazylak and N. Djilali, *Journal of Power Sources*, 2007, **171**, 706-717.
37. M. M. Mezedur, M. Kaviany and W. Moore, *Aiche Journal*, 2002, **48**, 15-24.
38. R. Fluckiger, S. A. Freunberger, D. Kramer, A. Wokaun, G. G. Scherer and F. N. Buchi, *Electrochimica Acta*, 2008, **54**, 551-559.
39. D. R. Baker, D. A. Caulk, K. C. Neyerlin and M. W. Murphy, *Journal of the Electrochemical Society*, 2009, **156**, B991-B1003.
40. T. E. Springer, T. A. Zawodzinski, M. S. Wilson and S. Gottesfeld, *Journal of the Electrochemical Society*, 1996, **143**, 587-599.
41. D. A. G. Bruggeman, *Annalen Der Physik*, 1935, **24**, 636-664.
42. A. T. Corey, *Producer's Monthly*, 1954, **18**, 38.
43. R. H. Brooks and A. T. Corey, *Hydrology Papers*, 1964.
44. M. T. Vangenuchten, *Soil Science Society of America Journal*, 1980, **44**, 892-898.
45. V. Gurau, M. J. Bluemle, E. S. De Castro, Y. M. Tsou, J. A. Mann and T. A. Zawodzinski, *Journal of Power Sources*, 2006, **160**, 1156-1162.
46. A. Z. Weber, *Journal of Power Sources*, 2010, **195**, 5292-5304.
47. P. Cheung, J. D. Fairweather and D. T. Schwartz, *Journal of Power Sources*, 2009, **187**, 487-492.
48. K. E. Thompson, *Aiche Journal*, 2002, **48**, 1369-1389.
49. E. Unsal, J. H. Dane, P. Schwartz and G. V. Dozier, *Simulation-Transactions of the Society for Modeling and Simulation International*, 2006, **82**, 499-510.
50. V. P. Schulz, J. Becker, A. Wiegmann, P. P. Mukherjee and C. Y. Wang, *Journal of the Electrochemical Society*, 2007, **154**, B419-B426.
51. C. R. Ethier, *Aiche Journal*, 1991, **37**, 1227-1236.
52. X. W. Shan and H. D. Chen, *Physical Review E*, 1993, **47**, 1815-1819.
53. C. Pan, M. Hilpert and C. T. Miller, *Water Resources Research*, 2004, **40**, 14.
54. P. K. Sinha, P. P. Mukherjee and C. Y. Wang, *Journal of Materials Chemistry*, 2007, **17**, 3089-3103.

55. N. S. Martys and H. D. Chen, *Physical Review E*, 1996, **53**, 743-750.
56. H. J. Vogel, J. Tolke, V. P. Schulz, M. Krafczyk and K. Roth, *Vadose Zone Journal*, 2005, **4**, 380-388.
57. Y. Deng and L. W. Lake, *Geofluids*, 2001, **1**, 11.
58. R. D. Hazlett, *Transport in Porous Media*, 1995, **20**, 21-35.
59. M. C. Leverett, *Transactions of the American Institute of Mining and Metallurgical Engineers*, 1941, **142**, 152-169.
60. K. S. Udell, *International Journal of Heat and Mass Transfer*, 1985, **28**, 485-495.
61. J. T. Gostick, M. W. Fowler, M. A. Ioannidis, M. D. Pritzker, Y. M. Volfkovich and A. Sakars, *Journal of Power Sources*, 2006, **156**, 375-387.
62. L. S. Penn and B. Miller, *Journal of Colloid and Interface Science*, 1980, **78**, 238-241.
63. K. G. Gallagher, R. M. Darling, T. W. Patterson and M. L. Perry, *Journal of the Electrochemical Society*, 2008, **155**, B1225-B1231.
64. I. R. Harkness, N. Hussain, L. Smith and J. D. B. Sharman, *Journal of Power Sources*, 2009, **193**, 122-129.
65. J. D. Fairweather, P. Cheung, J. St-Pierre and D. T. Schwartz, *Electrochemistry Communications*, 2007, **9**, 2340-2345.
66. J. T. Gostick, M. A. Ioannidis, M. W. Fowler and M. D. Pritzker, Wettability and capillary behavior of fibrous gas diffusion media for polymer electrolyte membrane fuel cells, 2009.
67. C. Lim and C. Y. Wang, *Electrochimica Acta*, 2004, **49**, 4149-4156.
68. J. St-Pierre, *Journal of the Electrochemical Society*, 2007, **154**, B724-B731.
69. M. A. Hickner, N. P. Siegel, K. S. Chen, D. N. McBrayer, D. S. Hussey, D. L. Jacobson and M. Arif, *Journal of the Electrochemical Society*, 2006, **153**, A902-A908.
70. C. A. Volkert and A. M. Minor, *Mrs Bulletin*, 2007, **32**, 389-395.
71. M. D. Uchic, L. Holzer, B. J. Inkson, E. L. Principe and P. Munroe, *Mrs Bulletin*, 2007, **32**, 408-416.
72. J. R. Wilson, W. Kobsiriphat, R. Mendoza, H. Y. Chen, J. M. Hiller, D. J. Miller, K. Thornton, P. W. Voorhees, S. B. Adler and S. A. Barnett, *Nature Materials*, 2006, **5**, 541-544.
73. I. Manke, C. Hartnig, M. Grunerbel, W. Lehnert, N. Kardjilov, A. Haibel, A. Hilger, J. Banhart and H. Riesemeier, *Applied Physics Letters*, 2007, **90**, 3.
74. J. Eller, T. Rosen, F. Marone, M. Stampanoni, A. Wokaun and F. N. Buechi, *Journal of the Electrochemical Society*, 2011, **158**, B963-B970.
75. R. Flueckiger, F. Marone, M. Stampanoni, A. Wokaun and F. N. Buechi, *Electrochimica Acta*, 2011, **56**, 2254-2262.
76. P. K. Sinha, P. Halleck and C. Y. Wang, *Electrochemical and Solid State Letters*, 2006, **9**, A344-A348.
77. I. Manke, C. Hartnig, M. Grunerbel, J. Kaczerowski, W. Lehnert, N. Kardjilov, A. Hilger, J. Banhart, W. Treimer and M. Strobl, *Applied Physics Letters*, 2007, **90**, 3.
78. A. Turhan, K. Heller, J. S. Brenizer and M. M. Mench, *Journal of Power Sources*, 2006, **160**, 1195-1203.
79. K. R. Minard, V. V. Viswanathan, P. D. Majors, L. Q. Wang and P. C. Rieke, *Journal of Power Sources*, 2006, **161**, 856-863.
80. S. Tsushima, K. Teranishi and S. Hirai, *Electrochemical and Solid State Letters*, 2004, **7**, A269-A272.

81. D. Wildenschild, J. W. Hopmans, C. M. P. Vaz, M. L. Rivers, D. Rikard and B. S. B. Christensen, *Journal of Hydrology*, 2002, **267**, 285-297.
82. C. S. Willson, R. W. Stacey, K. Ham and K. E. Thompson, in *Developments in X-Ray Tomography IV*, ed. P. SPIE, SPIE, Bellingham, WA, 2004, vol. 5535, p. 101.
83. A. Groso, R. Abela and M. Stampanoni, *Optics Express*, 2006, **14**, 8103-8110.
84. J. T. Gostick, H. P. Gunterman, B. Kienitz, J. Newman, Alastair MacDowell and A. Z. Weber, *ECS Transactions*, 2010, **33**, 1407.
85. J. Becker, R. Flueckiger, M. Reum, F. N. Buechi, F. Marone and M. Stampanoni, *Journal of the Electrochemical Society*, 2009, **156**, B1175-B1181.
86. A. V. Bronnikov, *Journal of the Optical Society of America a-Optics Image Science and Vision*, 2002, **19**, 472-480.
87. R. H. Brooks and A. T. Corey, *Hydrology Papers*, 1964.
88. K. Kinoshita and P. Stonehart, in *Modern Aspects of Electrochemistry*, ed. J. O. M. B. a. B. E. Conway, Plenum Press, New York, 1977, vol. 12, ch. 4, pp. 183-266.
89. D. Kramer, S. A. Freunberger, R. Fluckiger, I. A. Schneider, A. Wokaun, F. N. Buchi and G. G. Scherer, *Journal of Electroanalytical Chemistry*, 2008, **612**, 63-77.
90. M. M. Tomadakis and S. V. Sotirchos, *Aiche Journal*, 1991, **37**, 74-86.
91. M. M. Tomadakis and S. V. Sotirchos, *Aiche Journal*, 1993, **39**, 397-412.
92. M. M. Tomadakis and T. J. Robertson, *Journal of Composite Materials*, 2005, **39**, 163-188.
93. L. Berhan and A. M. Sastry, *Physical Review E*, 2007, **75**, 8.
94. B. Markicevic, T. D. Papathanasiou and Kr, *Physics of Fluids*, 2002, **14**, 3347-3349.
95. J. M. Hakanson, S. Toll, T. S. Lundstrom and Qv, *Textile Research Journal*, 2005, **75**, 304-311.
96. M. P. Sobera and C. R. Kleijn, *Physical Review E*, 2006, **74**.
97. V. Sygouni, C. D. Tsakiroglou and A. C. Payatakes, *Physics of Fluids*, 2006, **18**, 15.
98. O. Chapuis, M. Prat, M. Quintard, E. Chane-Kane, O. Guillot and N. Mayer, *Journal of Power Sources*, 2008, **178**, 258-268.

Appendix

A.1 LANL CL ink production protocol

Need:

- Small vial
- Stir bar
- 5% Nafion solution 1100 EW
- 20% Pt on Vulcan XC-72
- Glycerol
- 1 M Tetrabutylammonium hydroxide (TBAOH) in methanol
- Stir table
- Balance
- Oven

Standard ink—
Amounts listed will produce approximately 60 mg of 20% Pt/C catalyst.

1. Measure 0.5 g of 5% Nafion solution into a small vial with a stir bar. Record the weight of the Nafion (wNaf) and cap the vial.

2. For the standard 5:2 ink (5:2 catalyst to Nafion), divide wNaf by 20 and multiply by 5/2. This is the weight of Pt/C needed. Add this to the vial and record weight. Stir extensively for at least 1 hour.

3. Add glycerol, roughly half of wNaf. Record the weight and stir for another hour. Glycerol prevents drying of the solution and clumping when TBAOH is added.

4. Add TBAOH using a micropipette. The aim is to add roughly 1/3 excess of TBAOH and is included in the calculations. Using 1 M TBAOH, you want 0.050 g of 1 M TBAOH per gram of 5% Nafion solution. Hence for 0.5 g of Nafion, 0.025 g of TBAOH would be added. This can be approximated as 25 microliters. Set a pipette for this amount and add small amounts until the desired amount is added. Record the addition and stir for at least 1 hr.

5. Add a similar amount of glycerol as was added in step 3, but do not exceed more than 1.2 times wNaf for the total addition. Record the addition and stir overnight. If any lumps remain, grind them with a stir rod or use a sonicator until there are no more lumps or graininess.

To calculate the precious metal loading of the dried ink, dried 5:2 20% Pt/C:Nafion ink is 14.3% Pt by weight.

A.2 Preconditioning Nafion

Cut membrane to desired size prior to treatment.

Sodium form membrane—

1. Boil Nafion in 3% H_2O_2 for 1 h (for 1 L solution, add deionized water to 100 ml of 30% H_2O_2 solution).
2. Rinse well in deionized water.
3. Boil in deionized water for 1 h.
4. Boil in 1% NaOH by weight for 1 h.
5. Rinse well in deionized water.
6. Boil in deionized water for 1 h.
7. Store membrane in deionized water until needed.

Proton form membrane—

Follow steps 1-3 above and proceed to step a.

a. Boil Nafion in 0.5 M H_2SO_4 for 1 hr.
b. Rinse well in deionized water.
c. Boil in deionized water for 1 hr.
d. Store membrane in deionized water until needed.

A.3 Preparation of MEAs

Need:

- PTFE blanks: sandwich 10 mil reinforced white silicone fabric between two 10 mil (254 μm) fiberglass reinforced PTFE fabrics with adhesive backing
- Fine paintbrush
- Tongs/tweezers
- Isopropanol
- Deionized water
- 0.5 M H_2SO_4
- PTFE spray, e.g. Aervoe Industries, Dry Film Lubricant 6075
- 2 Furon or fiberglass reinforced PTFE fabrics, larger than membrane
- 2 thin stainless steel sheets, e.g. 1/16" (1.6 mm)
- 5 lbs (2 kg) weight, e.g. a standard brick
- Balance
- Oven
- Hot press

1. Clean PTFE blanks with isopropanol and DI water.
2. Dry the blanks for 10 min at 140 °C.
3. Weigh the blanks separately and record the weight.
4. Spray the blanks with PTFE spray to create a thin, even coating of PTFE. Let dry for 10 min at room temperature.
5. Calculate the weight of the completely dry catalyst needed to achieve the desired weight loading.
6. Using tongs to hold the blank in place and dipping only the tip of the brush into the catalyst ink, brush a thin but even layer of ink onto the blank. Brush in one direction only, e.g. always brush from left to right. Keep track of the orientation.
7. Dry the painted blanks at 140 °C in an oven until the layer is completely dry, typically 30 to 60 min.
8. Weigh the blanks and compare the weight of the dried catalyst layer on the blanks to the desired weight.
9. If the desired weight is not reached, rotate the sample 90°, and repeat steps 6, 7, and 8 until the desired weight is achieved (see below). Allow the sample to dry overnight after the final painting.

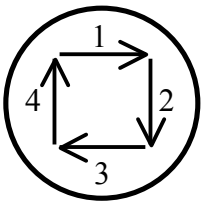

Paint the ink in strokes in the direction of 1 only, and then dry.
Rotate the sample so that the next layer is being applied in direction 2 only.
Continue this process for as many layers as necessary.

10. If the desired weight is reached, proceed with drying the Nafion membrane. The Nafion must be in sodium form such that the glass-transition temperature is higher. This leads to

better properties for hot pressing the materials. Dry the Nafion at 130 °C for 5 min on a vacuum hot plate.

11. Preheat hot press to 210 °C.
12. Place a thin PTFE sheet or PTFE-coated fiberglass sheet on top of a thin sheet of stainless steel. Position the MEA materials such that the painted electrode side of the two blanks is on either side of the dried Nafion, Place another PTFE or PTFE-coated sheet on the top and sandwich the stack with a second metal sheet.
13. Center the metal sheet assembly in the hot press and press with
    a) 600 lbs (272 kg) for 5 cm^2
    b) 6000 lbs (2720 kg) for 50 cm^2
    c) in general, 120 lbs/cm^2 (260 bar).
14. Press for 5 min.
15. After 5 min, remove metal sheet assembly, and let cool for 10 min under the 5 lbs (2 kg) weight.
16. Remove the sandwich from the metal sheets.
17. Peel off PTFE blanks from Nafion membrane by moving the edges carefully up and down to release the catalyst layer from the blanks.
18. Weigh the PTFE blanks separately to calculate the real Pt loading for anode and cathode.
19. Boil the MEA for 1 h in 0.5 M H_2SO_4 to change from sodium form to proton form.
20. Rinse MEA in deionized water.
21. Boil for 1 h in deionized water.
22. Dry MEA at 60 °C for 20 to 30 min on a vacuum hot plate. Turn on the vacuum first and remove the worst wrinkles, then turn on heater.
23. If MEA is still wrinkled after drying, put it back in deionized water until it relaxes, then repeat 22.
24. Store dried MEA in closed plastic bag until used.